Carbohydrate Polymers 302 (2023) 120395

Contents lists available at ScienceDirect

Carbohydrate Polymers

journal homepage: www.elsevier.com/locate/carbpol

3D bioprinted colorectal cancer models based on hyaluronic acid and signalling glycans

Francesca Cadamuro [a], Laura Marongiu [a], Michele Marino [c], Nicolò Tamini [d,e], Luca Nespoli [d,e], Nicola Zucchini [e], Alberta Terzi [f], Davide Altamura [f], Zirui Gao [g], Cinzia Giannini [f], Greta Bindi [h], Andrew Smith [h], Fulvio Magni [h], Sabrina Bertini [i], Francesca Granucci [a], Francesco Nicotra [a], Laura Russo [a,b,*]

[a] Department of Biotechnology and Biosciences, University of Milano-Bicocca, 20126 Milan, Italy
[b] CÚRAM, SFI Research Centre for Medical Devices, National University of Ireland Galway, H91TK33 Galway, Ireland
[c] Department of Civil Engineering and Computer Science, University of Rome Tor Vergata, 00133 Rome, Italy
[d] School of Medicine and Surgery, University of Milano-Bicocca, 20126 Milan, Italy
[e] ASST San Gerardo Hospital, 20900 Monza, Italy
[f] Institute of Crystallography, National Research Council, v. Amendola 122/O, 70126 Bari, Italy
[g] Paul Scherrer Institute, Villigen PSI 5232, Switzerland
[h] Department of Medicine and Surgery, Proteomics and Metabolomics Unit, University of Milano-Bicocca, 20854 Vedano al Lambro, Italy
[i] G. Ronzoni Institute for Chemical and Biochemical Research, 20133 Milan, Italy

ARTICLE INFO

Keywords:
Hyaluronic acid
Glycosignature
3D bioprinting
Bioresponsive hydrogels
Colorectal cancer models

ABSTRACT

In cancer microenvironment, aberrant glycosylation events of ECM proteins and cell surface receptors occur. We developed a protocol to generate 3D bioprinted models of colorectal cancer (CRC) crosslinking hyaluronic acid and gelatin functionalized with three signalling glycans characterized in CRC, 3′-Sialylgalactose, 6′-Sialylgalactose and 2′-Fucosylgalactose. The crosslinking, performed exploiting azide functionalized gelatin and hyaluronic acid and 4arm-PEG-dibenzocyclooctyne, resulted in biocompatible hydrogels that were 3D bioprinted with commercial CRC cells HT-29 and patient derived CRC tumoroids. The glycosylated hydrogels showed good 3D printability, biocompatibility and stability over the time. SEM and synchrotron radiation SAXS/WAXS analysis revealed the influence of glycosylation in the construct morphology, whereas MALDI-MS imaging showed that protein profiles of tumoroid cells vary with glycosylation, indicating that sialylation and fucosylation of ECM proteins induce diverse alterations to the proteome of the tumoroid and surrounding cells.

1. Introduction

3D tissue models represent an innovative tool to study human pathologies and to develop personalized therapeutic strategies (Sensi et al., 2020). Nowadays, 3D bioprinting represents a tunable, efficient, economical and easy to standardize technique to produce 3D advanced tissue model (Langer et al., 2019; Mota et al., 2020).

To closely mimic the in vivo extracellular matrix (ECM) of a specific tissue, synthetic 3D scaffolds need to recapitulate their morphological and chemical properties, in particular stiffness and specific signalling biomolecules (Chen et al., 2022; Kawai et al., 2020; Nicolas et al., 2020; Sbirkov et al., 2021). Indeed, native ECM is a complex network of structural proteins, glycoproteins, glycosaminoglycans and proteoglycans, playing an important biochemical and biomechanical role inducing different physiological and pathological cell fates (Sampaolesi et al., 2019; Wiig et al., 2008). Alterations in glycosylation regulate the development and progression of cancer (Jung et al., 2021; Luo et al., 2021; Pinho & Reis, 2015; Venkitachalam et al., 2016). In colorectal cancer (CRC) a differential production of collagen VI and hyaluronic acid has been observed (Giussani et al., 2019). Noteworthy, in the tissue

* Corresponding author at: Department of Biotechnology and Biosciences, Piazza della Scienza 2, 20126 Milan, Italy.
E-mail addresses: f.cadamuro@campus.unimi.it (F. Cadamuro), laura.marongiu@unimib.it (L. Marongiu), m.marino@ing.uniroma2.it (M. Marino), luca.nespoli@unimib.it (L. Nespoli), n.zucchini@asst-monza.it (N. Zucchini), alberta.terzi@ic.cnr.it (A. Terzi), davide.altamura@ic.cnr.it (D. Altamura), zirui.gao@psi.ch (Z. Gao), cinzia.giannini@ic.cnr.it (C. Giannini), g.bindi@campus.unimib.it (G. Bindi), andrew.smith@unimib.it (A. Smith), fulvio.magni@unimib.it (F. Magni), bertini@ronzoni.it (S. Bertini), francesca.granucci@unimib.it (F. Granucci), francesco.nicotra@unimib.it (F. Nicotra), laura.russo@unimib.it (L. Russo).

https://doi.org/10.1016/j.carbpol.2022.120395
Received 29 September 2022; Received in revised form 21 November 2022; Accepted 22 November 2022
Available online 30 November 2022

surrounding CRC patient derived tumors, the glycosignature has been recently characterized showing aberrant 6-sialyllation and decrease in fucosylation (Boyaval et al., 2021; Li & Ding, 2019; Peixoto et al., 2019; Rodrigues et al., 2021).

3D bioprinting is a valid technique to develop advanced 3D tissue models with a precise, rapid and personalized specificity (Alheib et al., 2021; Kačarević et al., 2018). 3D CRC models were bioprinted using natural biopolymers, such as alginate with tethered RGD (Sbirkov et al., 2021), or decellularized ECM (Han et al., 2022), with Caco-2 cells which aggregate in clusters with malignant histopathological appearance and show significant expression of stemness and differentiation markers. Other models made by collagen (Chen, Cheng, et al., 2020; Nyga et al., 2013) or GelMA (Burkholder-Wenger et al., 2022) were 3D printed and HCT116 cells were subsequently seeded on top, demonstrating the advantages of 3D versus 2D cell culture in promoting physiological functions. Considering the role of glycosignature in CRC progression and metastatisation, it is important to glycosylate the in vitro model to faithfully mimic the in vivo tissue (Magalhães et al., 2017; Peixoto et al., 2019).

The hypothesis of this work is that differential ECM glycosignatures influence single cell proteome in 3D bioprinted colorectal constructs.

We developed protocols to generate 3D-printable bioinks functionalized with different signalling glycans. We exploited them to generate in vitro models of CRC, even if the approach is suitable for any other tissue model.

The two major components of ECM, gelatin and hyaluronic acid, were selected as starting biomaterials. Gelatin provides cell adhesion properties by the RGD sequence (Davidenko et al., 2016; Russo et al., 2016) whereas hyaluronic acid maintains the water content of the tissue and interact with specific cells receptor overexpressed in CRC, such as CD44 and RHAMM (Amorim et al., 2021; Lugli et al., 2006).

Three glycans characterized in CRC ECM, 3′-Sialylgalactose, 6′-Sialylgalactose and 2′-Fucosylgalactose (Boyaval et al., 2021; Wang et al., 2022), were covalently attached to the lysine residues of gelatin by a reductive amination in which the glucose terminus loses the pyranosidic structure and acts as linker for conjugation (see Scheme 1).

To generate 3D-printed construct with tailorable properties, the crosslinking between gelatin and hyaluronic acid must be controlled. We functionalised both with an azido group and performed the crosslinking exploiting 4arm-PEG-DBCO (Fig. 1). Different formulations were tested changing the hydrogel components ratio. The constructs were characterized for their bioprintability, morphological and structural properties. The biocompatibility and bioresponsiveness were determined by LIVE/DEAD assay with human colon cancer cells HT29. Subsequently the hydrogels were bioprinted with CRC patient–derived tumoroids.

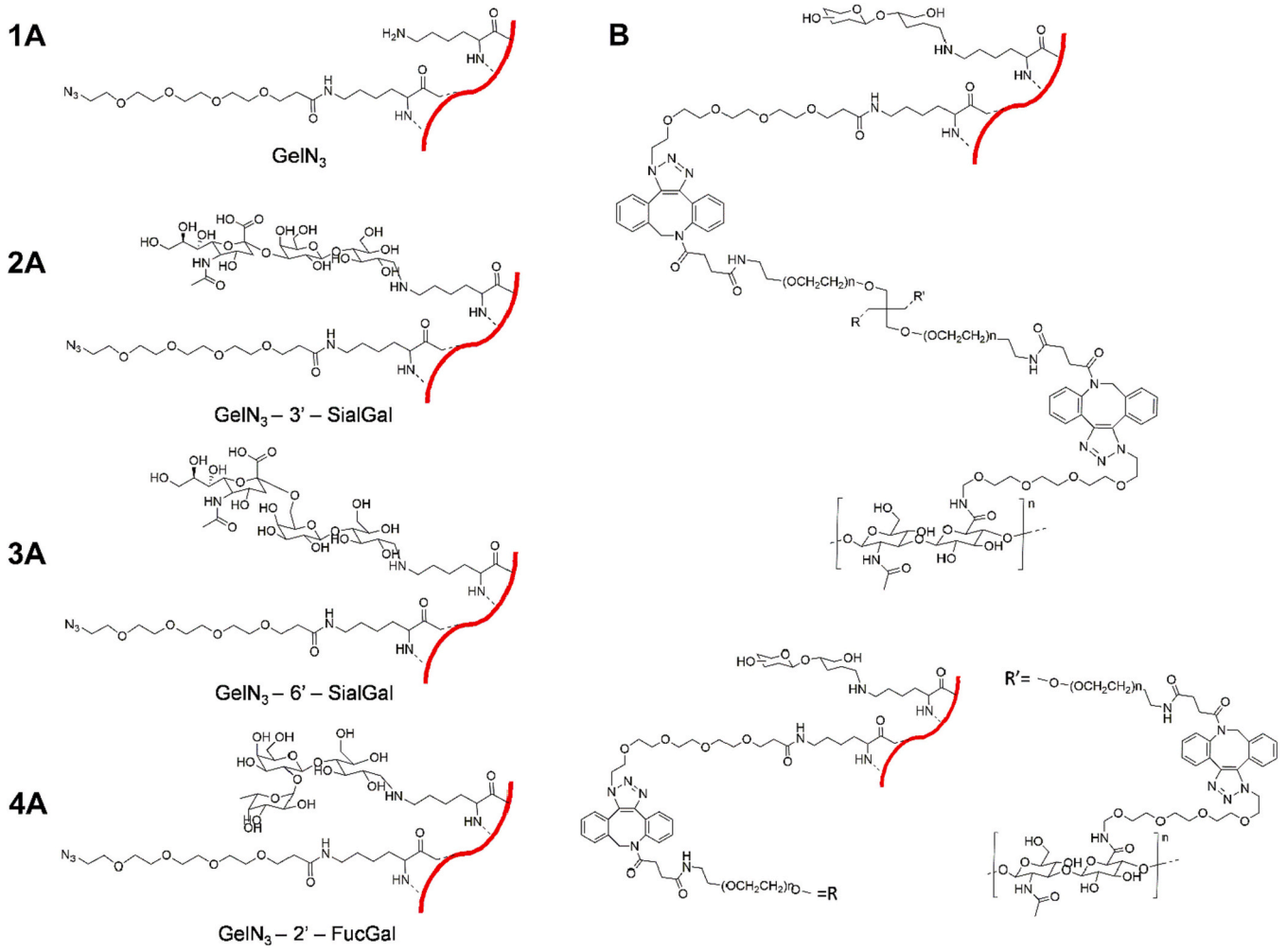

Scheme 1. Schematic structures of **1A**) gelatin functionalized with azide group (Gel—N_3), **2A**) gelatin functionalized with azide group and 3′-Sialylgalactose ($GelN_3$-3′-SialGal), **3A**) gelatin functionalized with azide group and 6′-Sialylgalactose ($GelN_3$-6′-SialGal), **4A**) gelatin functionalized with azide group and 2′-Fucosylgalactose ($GelN_3$-2′-FucGal); **B**) final hydrogel structure obtained crosslinking glyconjugate-azide-gelatin derivatives and azide-conjugate hyaluronic acid with 4arm-PEG-DBCO.

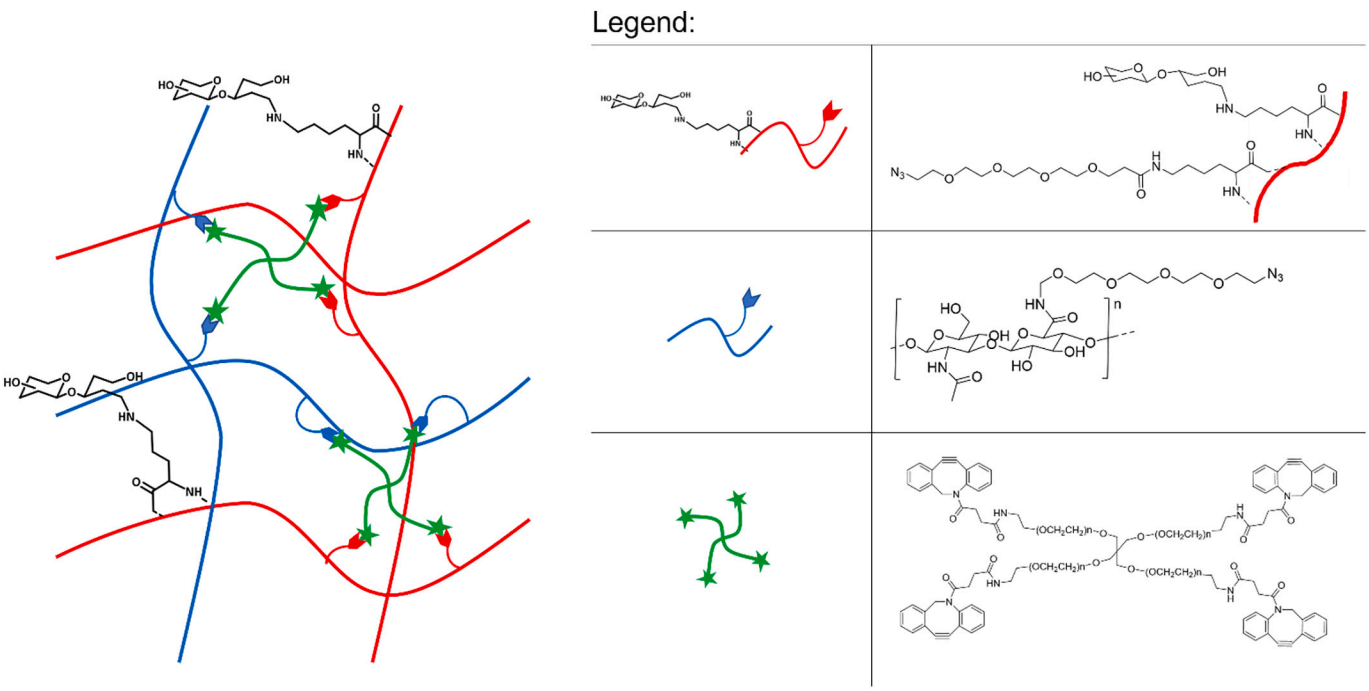

Fig. 1. Schematic structure of hybrid hydrogel.

2. Materials and method

2.1. Materials

Gelatin from porcine skin type A (G2500, Sigma Aldrich) (Magli et al., 2021), N-hydroxysuccinimide (NHS), phosphate buffered saline (PBS), N_3-PEG_4-COOH, 4arm-PEG-DBCO, $NaBH_3CN$, N_3-$PEGNH_2$, Hyaluronidase from bovine testes (Type I—S), ninhydrin, hematoxylin, eosin, McCoy's 5A medium, L-glutamine, Fetal Bovine Serum, penicillin, streptomycin, live/dead Cell viability Assay kit (CBA415) were purchased from Sigma-Aldrich. 1-Ethyl-3-(3-dimethylaminopropyl)carbodiimide (EDC), 4-(4,6-Dimethoxy-1,3,5-triazin-2-yl) (DMTMM) were purchased from TCI; Alexa Fluor 647 Phalloidin, 4′,6-diamidino-2-phenylindole (DAPI) from Thermo Fisher Scientific; CD133/1 (AC133) pure human from Miltenyi Biotec; Human LGR5/GPR49 Antibody (MAB8078) was purchased from Bio-techne brand; Intesticult medium from Stem cell technologies; Buffer solution pH 6.0 (20 °C) citric acid / sodium hydroxyde solution with fungicide from Fisher Scientific; Hyaluronic acid (YH05852 average MW 1.0–2.0 million Da) from Carbosynth Ltd.; Human colon cancer cells HT29 from LGC Standards S.r.L. 2′-fucosyllactose, 3′-sialyllactose, 6′-sialyllactose were kindly provided by Chr Hansen A/S (Hørsholm, Denmark).

2.2. Azide functionalized gelatin ($GelN_3$)

N_3-PEG_4-COOH (50 mg, 0.171 mmol) was dissolved in PBS 5.5 (5 mL) in a bottom round flask at rt. Then, EDC (66 mg, 0.342 mmol) and NHS (40 mg, 0.342 mmol) were added under gentle stirring. Meanwhile, gelatin type A (250 mg, 0.085 mmol) was dissolved in PBS 5.5 (15 mL) in a falcon. After 45 min, the gelatin solution was added dropwise into the PEG solution. The reaction was stirred overnight at 37 °C. Further EDC (66 mg, 0.342 mmol) and NHS (40 mg, 0.342 mmol) were added and the mixture was stirring for 4 h, then dialyzed with a 14 kDa cellulose membrane against NaCl 0.1 M for 1 day and then against milli-Q water for 2 days. The obtained azidated gelatin ($GelN_3$) was lyophilized and stored at −20 °C before use.

2.3. One step glyco- and azide functionalization of gelatin ($GelN_3$-2′-FucGal, $GelN_3$-3′-SialGal and $GelN_3$-6′-SialGal)

To a solution of N_3-PEG_4-COOH (50 mg, 0.171 mmol) in PBS 5.5 (5 mL), EDC (66 mg, 0.342 mmol) and NHS (40 mg, 0.342 mmol) were added. After 45 min under stirring gelatin type A (250 mg, 0.085 mmol) dissolved in PBS 5.5 (15 mL) was added dropwise. The reaction was stirred overnight at 37 °C, then further 0.342 mmol of EDC and 0.0342 mmol of NHS were added and the mixture was stirring at 37 °C for 4 h. The reductive amination was then performed under stirring at 37 °C overnight with 8.5 mmol of 2′-fucosyllactose, 3′-sialyllactose, and 6′-sialyllactose, one for each batch, by adding $NaBH_3CN$ (293 mg, 4.25 mmol). Dialysis with a 14 kDa cellulose membrane against NaCl 0.1 M for 1 day, and then against milli-Q water for 2 days, and lyophilization provide $GelN_3$-3′-SialGal, $GelN_3$-6′-SialGal and $GelN_3$-2′-FucGal which were characterized by FT-IR analysis and NMR analysis.

2.4. Azide functionalization of hyaluronic acid (HAN_3)

DMTMM (146 mg, 0.572 mmol) was added to a stirred solution of hyaluronic acid (100 mg, 0.264 mmol) in MES buffer pH 5.5 (20 mL), after 40 min N_3-PEG-NH_2 (115 mg, 0.572 mmol) was added and the solution was stirred overnight, dialyzed with a 14 kDa cellulose membrane against NaCl 0.1 M for 2 days and then against milli-Q water for 2 days. The obtained HAN_3 was lyophilized and stored at −20 °C before use.

2.5. Analytical instruments, FT-IR and NMR

FT-IR were performed after freeze drying using a Nicolet iS20, Thermo Scientific; ^1H NMR were performed using a Varian Mercury 400 M Hz, dissolving the sample in D_2O with 0.05 % (wt%) TMSP at a concentration of 7 mg/mL.

2.6. Ninhydrin assay

The gelatin glyco-functionalization degree was determined quantifying the unreacted lysine residues with ninhydrin assay. 250 μL of a

solution of each gelatin sample (2 mg/mL in citricacid/sodium hydroxide buffer at pH 6.0) were mixed with 125 μL of a freshly prepared solution of ninidrin (2 % *w/V* in 95 % ethanol) and left into boiling water for 10 min. Then 125 μL of ethanol were added and 100 μL of each final solution were posed into 96-microwell plates and the absorbance values (570 nm) measured with UV–Vis SPECTROstar Nano BMG LABTECH. Three replicates were analyzed and results compared to a standard curve based on glycine. Buffer solution pH 6.0 (20 °C) (citric acid/sodium hydroxide solution) was used as blank.

2.7. Inks and bioinks formation

2.7.1. Hyaluronic acid – Gelatin inks

$GelN_3$, $GelN_3$-2′-FucGal, $GelN_3$-3′-SialGal and $GelN_3$-6′-SialGal (28 mg) separately dissolved in filtered PBS 7.4 (0.3 mL) at 37 °C was mixed to a solution of HAN_3 (2 mg) in PBS 7.4 (0.4 mL). Then 4armPEG-DBCO (10 mg) dissolved in sterile PBS 7.4 (0.3 mL) was added and the solution was vortex for 1 min at 1600 rpm until complete gelation occurred. In this way the bioinks defined as HA-Gel (1), HA-Gel-2′-FucGal (2), HA-Gel-3′-SialGal (3) and HA-Gel-6′-SialGal (4) were obtained.

2.7.2. Hyaluronic acid – Gelatin bioinks

The solutions of HAN_3 (2 mg in 0.3 mL PBS 7.4), $GelN_3$, $GelN_3$–2′-FucGal, $GelN_3$–3′-SialGal and $GelN_3$-6′-SialGal (28 mg in 0.3 mL PBS 7.4), were sterilized under UV light for 30 min., maintained at 37 °C and mixed for bioprinting adding 4.5 * 10^6 HT29 cells suspended in 0.1 mL McCoy's 5A complete medium. Finally 4arm-PEG-DBCO (10 mg) dissolved in sterile PBS 7.4 was added and the mixtures were loaded in the bioprinter syringe and bioprinted after 2 min at 25–40 kPa with 21G conical bioprinter nozzle with Cellink INKREDIBLE 3D bioprinter.

2.8. Hydrogel characterization

2.8.1. Swelling

The swelling behaviors were evaluated in three replicates by immersing 0.5 mL of the hydrogel in 1 mL of PBS (containing 0,02 % *w/V* NaN_3) with pH 5.5 and 7.4 at 37 °C, and weighing at different time intervals.

Experimentally, the swelling ratio M_{exp} at time t was calculated as:

$$M_{exp}(t) = \frac{Wd(t) - Wi}{Wi} \quad (1)$$

where $Wd(t)$ is the weight of the swollen hydrogel at time t and Wi is the initial weight of the hydrogel.

The swelling is evaluated at equilibrium, that is at the end of the swelling process (when water adsorption is complete). The long-time dynamics of PBS uptake is mathematically described by means of the exponential law:

$$M_t(t) = M_\infty\left(1 - exp\left(-at^b\right)\right) \quad (2)$$

where $M_t(t)$ represents the swelling ratio at time t, M_∞ is the equilibrium swelling capacity (resulting $M_t \underset{t\to\infty}{\rightarrow} M_\infty$), and a and b are two model parameters (respectively, of units s^{-b} and dimensionless). Experimental data $M_{exp}(t)$ in Eq. (1) on the absorbed PBS are fitted by means of Eq. (2), thus obtaining the equilibrium swelling capacity M_∞ for different combinations of external conditions (e.g., pH) and polymer characteristics (e.g., functionalizations). The value of M_∞ gives an indirect measure of the available "open space" within the hydrogel network. Moreover, the short-time swelling dynamics $M_{st}(t)$ was described in terms of a power-law rule (depending on the power parameter n) and fitted towards the first 20 % of the absorbed PBS data (see Supplementary Information 1.3). Starting from $M_{st}(t)$, Fickian versus non-Fickian mechanisms could be evaluated, resulting $n \approx 0.5$ for the former and $0.5 < n < 1$ for the latter. This assessment gives an indirect information on the predominant swelling mechanism: either water diffusion within polymer pores alone (Fick-type) or in combination with macromolecular relaxation in the polymer network (non-Fick-type). From the ratio $M_{st}(t)/M_\infty$, the diffusion coefficient parameter D of PBS sorption could be also obtained (see Supplementary Information 1.3. Collectively, the afore-introduced quantities gave a comprehensive assessment of the features that can affect transport-driven processes in hydrogels, such as diffusion of nutrients and metabolites or migration and proliferation of cells.

2.8.2. Degradation test

The hydrogels degradation was tested with a solution of hyaluronidase (2,5 U/mL) (0,02 % *w/V* sodium azide was added as antibacteric). Briefly 0,3 mL of hydrogel was incubated at 37 °C with 1 mL of enzyme solution. At different time point the hydrogel was weighted and the mass loss calculated.

2.8.3. Rheological analysis

Rheological characterization was performed with a Modular Compact Rheometer MCR 92 (Anton Paar, GmbH, Graz, Austria) equipped with PP plane plate (50 mm). About 1,5 mL of each hydrogel was tested with viscosity test, amplitude sweep and frequency sweep at 37 °C, 0.1 mm gap. Viscosity measurement was performed in rotation mode, with shear rate in the range of 0.1–100 s^{-1} and least ten points per decade were acquired. Data were elaborated with RheoCompass™ software.

2.8.4. SEM analysis

The morphology and microstructure were evaluated using scanning electron microscopy using a ZEISS Gemini 500 field emission HR-SEM at voltage of 5 kV. Hydrogels were frozen in liquid nitrogen and then freeze dried. The samples were fixed with conductive adhesive on aluminum supports, and then coated with grafite.

2.8.5. Synchrotron radiation SAXS/WAXS

The samples printed as described in 2.7.1 and $GelN_3$ as control, were fixed with 4 % of paraformaldehyde (PFA) for 15 min. Then washed three times with PBS pH 7.4 and stored in PBS pH 7.4 with 0.02 % *w/V* of NaN_3. WAXS and SAXS scanning microscopies were performed, and data collected at cSAXS beamline of the Swiss Light Source in Villigen, Switzerland. The set-up is composed of liquid N_2 cooled fixed-exit Si (111) monochromator with a bendable second crystal for horizontal focusing, a bendable mirror for the rejection of higher X-ray energies and vertical focusing, a sample holder on a motorized 2D translation stage, a 7 m long evacuated flight tube between the sample and the detector for SAXS measurement, and a Pilatus 2 M detector downstream the scattered X-ray beam for data collection (Henrich et al., 2009). SAXS and WAXS measurements were performed using a monochromatic X-ray beam (λ = 0.09537 nm, E = 14.6 keV) focused down to about 10 μm (vertical) and 30 μm (horizontal) in size. Samples were studied in ultralene sachets sterilized in ethanol 70 % (*v*/v) and washed in phosphate-buffered saline (PBS) to remove ethanol. Each sample was placed into a sachet filled with a drop of 0.02 % w/V NaN_3 to avoid contaminations during analysis. The data collection was performed in continuous lines with 50 μm distance between lines. SAXS data were collected with the detector positioned 7098 mm downstream of the sample, while, for WAXS acquisition the flight tube was removed and data were collected with the detector positioned 210 mm downstream of the sample. The acquired SAXS and WAXS data were analyzed using multi-modal and segmentation approaches (Bunk et al., 2009; Lutz-Bueno et al., 2018) to find the most representative profiles for each investigated sample. Experimental data were calibrated based on standard measurements of silver behenate (SAXS) and Si, LaB6 (WAXS) samples, and folded into 1D profiles, after azimuthal integration.

2.9. Cell culture

2.9.1. HT29

Human colon cancer cells were cultured in McCoy's 5A complete medium supplemented with 10 % fetal bovine serum, 100 units/mL penicillin, and 100 mg/mL streptomycin. Cells were grown to 90 % confluence, trypsinized, plated in 75 cm^2 culture dishes at a density of 2 * 10^6 cells and incubated at 37 °C in a humidified atmosphere containing 5 % CO_2. The media was changed every two-three days.

2.9.2. Patient derived CRC tumoroids

Patient derived CRC tumoroids were derivated after tissue smashing using Gentle Cell Dissociation Reagent (Stemcell Technologies®). Fragment of tumor cryptes were cultured in Matrigel® Matrix (Corning ®) without phenol red, surrounded by IntestiCult™ medium. Tumoroids were cultured for at least 14 days to ensure adequate physiological growth.

2.10. 3D bioprinting

2.10.1. HT29 bioprinting

HA-Gel, HA-Gel-3′-SialGal, HA-Gel-6′-SialGal and HA-Gel-2′-FucGal with encapsuled HT29 were bioprinted in filled cylinder shape in 24 well plate at 25–40 kPa with 21G conical bioprinter nozzle with Cellink® INKREDIBLE+ 3D bioprinter. Next, the hydrogels were rinsed with media and cultured for 14 days. Samples were fixed with 4 % (*v*/v) paraformaldehyde and stained. Three replicates were prepared for each glyco-hydrogel.

2.10.2. CRC tumoroids bioprinting

HAN_3 (1,2 mg in 0.2 mL PBS 7.4), $GelN_3$ and $GelN_3$-6′-SialGal (16,8 mg in 0.15 mL PBS 7.4), and 4arm-PEG-DBCO (6 mg in powder) were sterilized under UV light for 30 min. Right before the bioprinting step each gelatin solution was mixed with HAN_3. 3 wells at confluence of CRC tumoroids were suspended in 0.1 mL IntestiCult™ medium and added to each gelatin solution. Finally 4arm-PEG-DBCO dissolved in 0,15 mL sterile PBS 7.4 was added and the mixture was loaded in the bioprinter syringe and bioprinted after 2 min at 25–40 kPa with 0.41 mm (inner diameter) conical bioprinter nozzle with pneumatic pressure of extrusion Cellink® INKREDIBLE+ 3D bioprinter. Hydrogels were printed in filled cylinder shape The hydrogels were rinsed with media and cultured for 14 and 21 days. Samples were fixed with 4 % (v/v) paraformaldehyde and stained.

2.11. Live/dead assay

The cytotoxicity of 3D cell-laden hydrogels was investigated with live/dead Cell viability Assay kit (CBA415-Merck Life Science). HT29 cell laden hydrogels were bioprinted in cylinder shape in 24 well plate. At 1, 3 and 7 days HT29 were stained with red-fluorescent ethidium homodimer-1 to indicate loss of plasma membrane integrity and green-fluorescent calcein-AM to indicate intracellular esterase activity for 20 min (37 °C, 5 % CO_2). Fluorescence images were collected with CELENA®S, Logos Biosystems.

2.12. Confocal analysis

The 3D custructs both with HT29 and CRC patient derived tumoroids after fixation with 4 % PFA were washed three times with PBS and then included in Tissue freezing medium and frozen at −80 °C. Finally the samples were cut with cryostat in slices of 20 μm. The slices were permeabilized with 0.5 % (*w*/*v*) Triton X solution, then stained with 0.66 μg/mL of Phalloidin and 0.4 μg/mL of DAPI. Images were acquired using a confocal microscope (Nikon A1R), where the blue and red colors indicated the nuclei and actin cytoskeleton respectively. For CD133 and LGR5 analyses of expression, slices were fixed with 4 % of PAF for 15, permeabilized with 0,1 % of Triton-X 100 and then incubated overnight with anti-LGR5 and anti-CD133 antibodies (1:100 dilution). After 3 washes in PBS, samples were incubated with second fluorescent antibodies for 1 h and then stained with 0.4 μg/mL of DAPI for 15 min. After mounting, samples were acquired with Thunder tissue instrument (Leica).

2.13. H&E staining

The 3D constructs with CRC patient derived tumoroids after fixation with 4 % *v*/*V* PFA were included in Tissue freezing medium and frozen at −80 °C. Finally the samples were cut with cryostat in slices of 20 μm. The slices were stained with hematoxylin for 5 min, washed running current water for 5 min, stained with eosin for 5 min and washed again with running water for 5 min. Then the samples were dihydrated with 20 immersion in progressively increasing (50 %, 70 % 80 % 95 % 100 %) EtOH acqueous solution. Finally samples were washed 3 min in Histoclear solution and Samples analyzed with Nano zoomer hamamatsu using Eukitt mounting medium.

2.14. MALDI-MS imaging analysis

Seven-micron-thick slices of each sample were cryosectioned and mounted onto conductive indium tin oxide glasses. Rehydration was performed with consecutive washes in 100 % ethanol (1 × 3 min), 70 % ethanol (1 × 3 min), and H_2O (2 × 2 min). A citric acid antigen retrieval (CAAR) was performed in a bath of citrate buffer (pH 5.9, 10 mM) at 97 °C for 45 min before being washed in H_2O (2 min) prior to enzyme application. Trypsin deposition (100 ng/μL) was performed using an iMatrixSpray automated spraying system and left in a humidity chamber overnight at 40 °C. Finally, a solution containing 10 mg/mL CHCA in 70 % acetonitrile with 0.1 % trifluoroacetic acid was deposited using a HTX TM-Sprayer.

All analyses were performed using a rapifleX MALDI Tissuetyper mass spectrometer (Bruker Daltonics, Bremen, Germany) equipped with a Smartbeam 3D laser operating at 10 kHz frequency. The measurements were performed in the *m/z* range from 700 to 3000, employing a beam scan setting of 16 μm and a raster sampling of 20 μm in both *x* and *y* dimensions, and accumulating 200 laser shots. External calibration was performed using Peptide Calibration Standard II (Bruker Daltonics, Bremen, Germany). Following the MALDI-MSI analysis, the tissue sections were washed with ethanol (70 and 100 %) and the slides were stained using hematoxylin and eosin (H&E).

Data files containing the individual spectra of each entire measurement region were imported into SCiLS Lab MVS 2021c (http://scils.de/; Bremen, Germany) and co-registration of the digital H&E image was performed in order to correlate sample morphology with the spatial proteomics data. Subsequently, spectra pre-processing and feature selection was performed and resulted in the detection of 242 protein features (*m*/z). These detected protein features were subsequently utilised for segmentation of the dataset using the bisecting k-means algorithm as well as unsupervised Principal Component Analysis (PCA). These approaches considered intensity variations of all the detected protein features in order to group spectra based upon the similarity. In particular, PCA was able to reduce the high complexity of the data and highlight proteomic differences between the cells produced by the 3D hydrogel tumoroids under different glycosylation conditions. The associated PCA Loadings Plot was then used to highlight a protein feature whose varied intensity contributed greatly to the separation observed in the PCA Score Chart and its discriminatory capability was confirmed using receiver operating characteristic analysis.

3. Results and discussion

3.1. Chemical modifications of polymers

This work proposes a protocol to generate 3D bioprinted models of CRC crosslinking hyaluronic acid and gelatin functionalized with signalling glycans specific for CRC. The protocol is suitable to generate 3D models of different tissues.

The strategy is based on the one step double functionalization of gelatin with glycans and with functional groups suitable for subsequent crosslinking with hyaluronic acid. The free amine groups of lysine residues of Gelatin have been first functionalized with N_3-PEG_4-COOH via carbodiimide chemistry and then with glycans (3′-siallylactose, 6′-sialyllactose and 2′-fucosyllactose) via reductive amination. In this way the time-consuming purification steps were reduced.

Each functionalised gelatin was characterized by FT-IR and ^{1}H NMR and the degree of glycosylation was calculated by ninhydrin assay (SI Fig. 4). In Fig. 2 the comparison between proton spectra of gelatin, Gel-N_3 and glyco-gelatin samples are reported.

^{1}H NMR spectra of glycosylated gelatins displayed the presence of the pick of -CH_2 protons next to amine of lysine residue in gelatin control spectra, which decreases its intensity in the azide-gelatin derivative between 2.9 ppm and 3.0 ppm and even more in glyco-conjugate sample spectra due to the functionalization of amine group of lysine residue. The signals of the sugar components are not observed due to both overlap with the peaks of the gelatin and because the content is very low since the lysin in the gelatin is about 5 % of lysine so we could attend maximum 5 % of derivatization including azide and glycol groups. In Table 1 SI are reported the chemical shift of amino acid protons in gelatin.

From the ninhydrin assay gelatins resulted functionalized for 2,9 % (*w/W*) with azide group and respectively for 0,15 % (w/W) with 3′-Sialylgalactose, and 0,2 % with 6′-Sialylgalactose and 2′-Fucosylgalactose, which correspond to a total degree of functionalization of the lysine residues of gelatin of: Gel-N_3 58%; GelN_3-3′-SialGal 62 %; GelN_3-6′-SialGal 61 %; GelN_3-2′-FucGal 61 % (considering 100 % the total amount of Lysine residue available).

The FT-IR spectra of glycosylated gelatins (Fig. 3A) showed an increase of the intensity of the pick at 1100 cm^{-1} due to the stretching of [C-O] bond of the glycan adduct. Variation respectively at 1580–1450 cm^{-1} and 1700–1600 cm^{-1} correspond to the modification of amine II and amine I, respectively. The azide group was identified at 2100 cm^{-1} (Fig. 3A). In the FT-IR spectra of HA-N_3 (Fig. 3B) the band of carbonyl of carboxylic group at 1620 cm^{-1} and an increase in the band at 1724 cm^{-1} due to the C═O stretching of the amide group in the product. At 1406 cm^{-1} can be identify the peak related to the stretching of C—N bond and at 1045 cm^{-1} the stretching of C—O relative to alcohol groups.

The chemical composition of HAN_3 was confirmed by ^{1}H NMR (Fig. 4). Around 3.2 and 4.2 ppm was possible to identify a broad multiplet with the signals of the protons of sugar rings and high peak corresponding to the -CH2 protons next to the oxygen of the PEG chain. At 1.9–2 ppm there was the signal corresponding to the methyl protons of the *N*-acetyl groups of HA.

Table 1
Formulation study with different biomaterial components ratio and concentration (total volume 1 mL).

CODE	Gelatin-N_3 (mg)	Hyaluronic acid – N_3 (mg)	4arm-PEG-DBCO (mg)	Printing pressure (kPa)	Printability
A	28	2	8	2–10	X
B	**28**	**2**	**10**	20–25	V
C	28	2	12	28–30	V
D	28	2	14	30–35	V
E	18	2	10	2–6	X
F	38	2	10	35–40	V

3.2. Hydrogel formulation

HA-N_3 was crosslinked with glycosylated gelatins with 4arm-PEG-DBCO as reported in Scheme 1 (SI) to obtain the final hydrogel (Scheme 1B). We performed preliminary study to find the best combination of biomaterial components ratio and concentrations (Table 1) to obtain the final hydrogel formulation. Comparing the printability, the hydrogel with a ratio HA/Gel/4armPEGDBCO of 1:14:5 (hydrogel B) resulted the best candidate, being printable with mild pressure and presenting higher stability in water, suitable conditions to stress as less as possible the cells during bioprinting and avoid premature degradation (Ouyang, 2022). Indeed, decreasing the PEG-linker concentration the hydrogel undergoes faster degradation in water and loses the printed shape quickly, while increase of the PEG-linker concentration results in higher stability but requires higher printing pressure, which generate stress to the cells. The gelatin/hyaluronic acid ratio is also determinant, a decrease of gelatin concentration compromises the gelation, whereas an increase leads to hydrogels requiring a higher printing pressure 30-40 kPa (Fig. 1 SI).

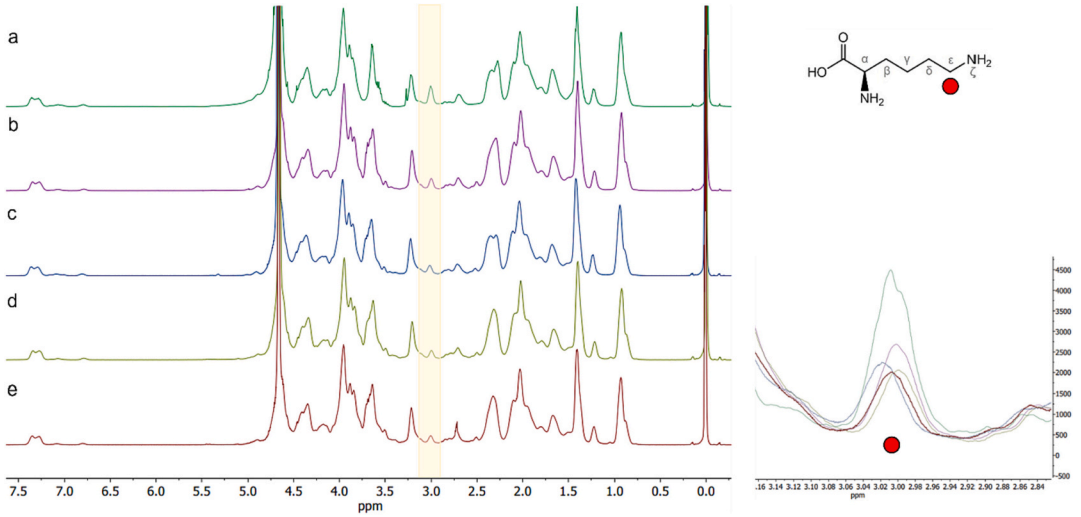

Fig. 2. ^{1}H NMR a) Gel CTRL, b) Gel—N_3, c) Gel-N_3-2′-FucGal, d) Gel-N_3-3′-SialGal and e) Gel-N_3-6′-SialGal.

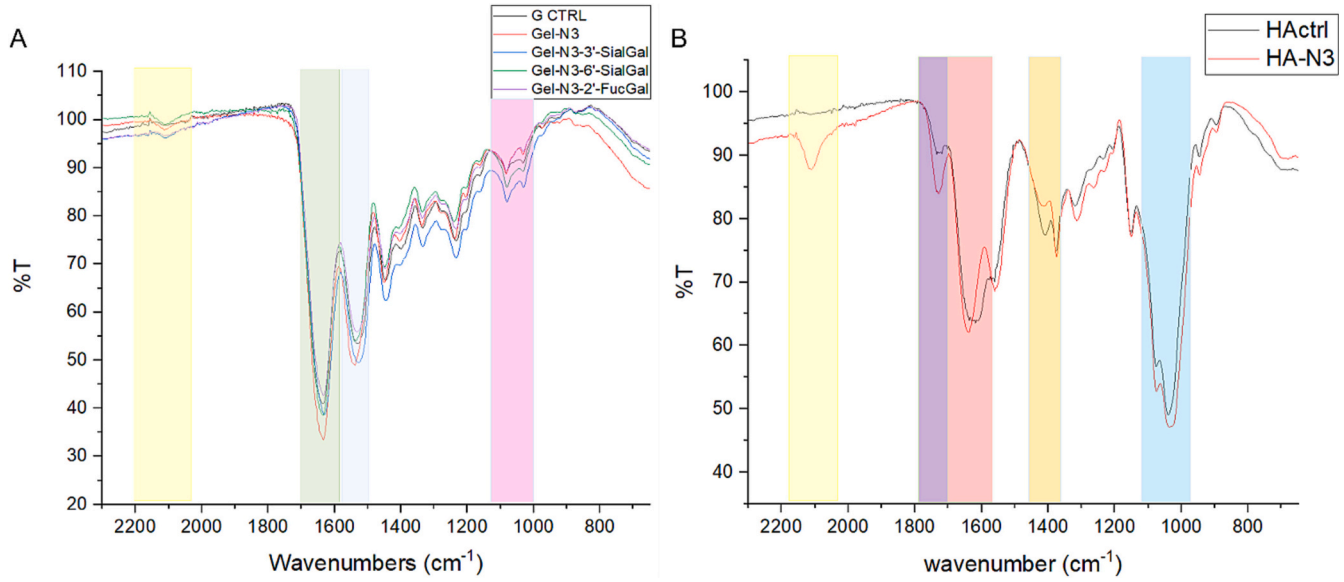

Fig. 3. A) FT-IR of glyco-functionalized gelatin samples; B) FT-IR spectra of HA-N_3.

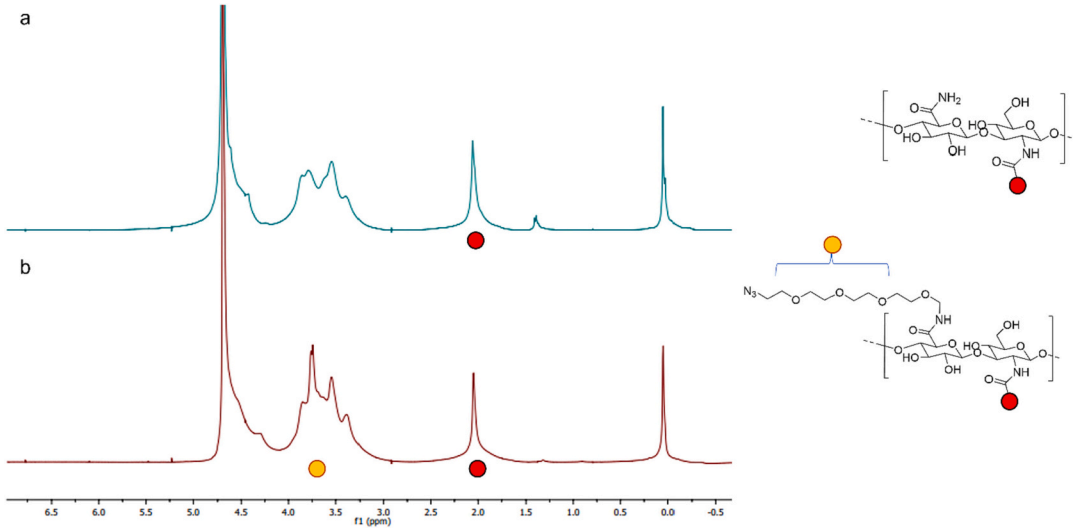

Fig. 4. ^{1}H NMR a) HA ctrl b), HA-N_3.

3.3. 3D bioprinting

3D bioprinted cell-laden hydrogels needs appropriate viscoelasticity, stiffness and swelling properties. To this aim we performed preliminary tests to find the best combination of reagents to generate hydrogels with printing pressure suitable for living cells, good stiffness and morphology of the printed constructs (Table 1). The hydrogels were printed with Cellink® INKREDIBLE+ 3D bioprinter, which guarantee printing replicates with the same size, shape and homogeneous dispersion of cells (SI Fig. 2).

The hydrogel with the best properties was selected to generate the glycosylated construct and investigate the role of ECM glycosylation in cell fate induction. To this purpose $GelN_3$, $GelN_3$-3′-SialGal, $GelN_3$-6′-SialGal, $GelN_3$-2′-FucGal were separately employed in combination with HA-N_3 to generate HA-Gel-3′-SialGal, HA-Gel-6′-SialGal and HA-Gel-2′-FucGal, which were 3D bioprinted with encapsulated commercial HT29. In this work, for the biological experiment, the biomolecular control has been preferred to the shape control, hydrogels were bioprinted in a filled cylinder geometry, obtaining homogeneous sample (Fig. 2 SI), in which cells could easily migrate, spread and colonize the hydrogel(Levato et al., 2020). The 3D bioprinting protocols was setup, the obtained constructs were deeply characterized and the hosted cell behaviour was analyzed.

3.4. Swelling

The stability in water of the four hydrogels (HA-Gel-3′-SialGal, HA-Gel-6′-SialGal and HA-Gel-2′-FucGal, and HA-Gel) was evaluated with a swelling test without cells at different pH (Fig. 5). Here, best-fitting functions $M_t(t)$ are also reported, as well as the resulting equilibrium swelling capacity M_∞ for the different case studies (Fig. 5A). Results on the short-range swelling dynamics are shown in Fig. 5B, where the best-fitting power law index n is reported. For non-functionalized HA-Gel, the value of n increases from pH = 5.5 to pH = 7.4. This phenomenon is typical of anionic polymer networks since macromolecular relaxation becomes more prominent in alkaline solutions, with non-Fickian transport increasing as the pH of the surrounding fluid increases above the pKa of the hydrogel. Contrarily, both HA-Gel-6′-SialGal and HA-Gel-2′-

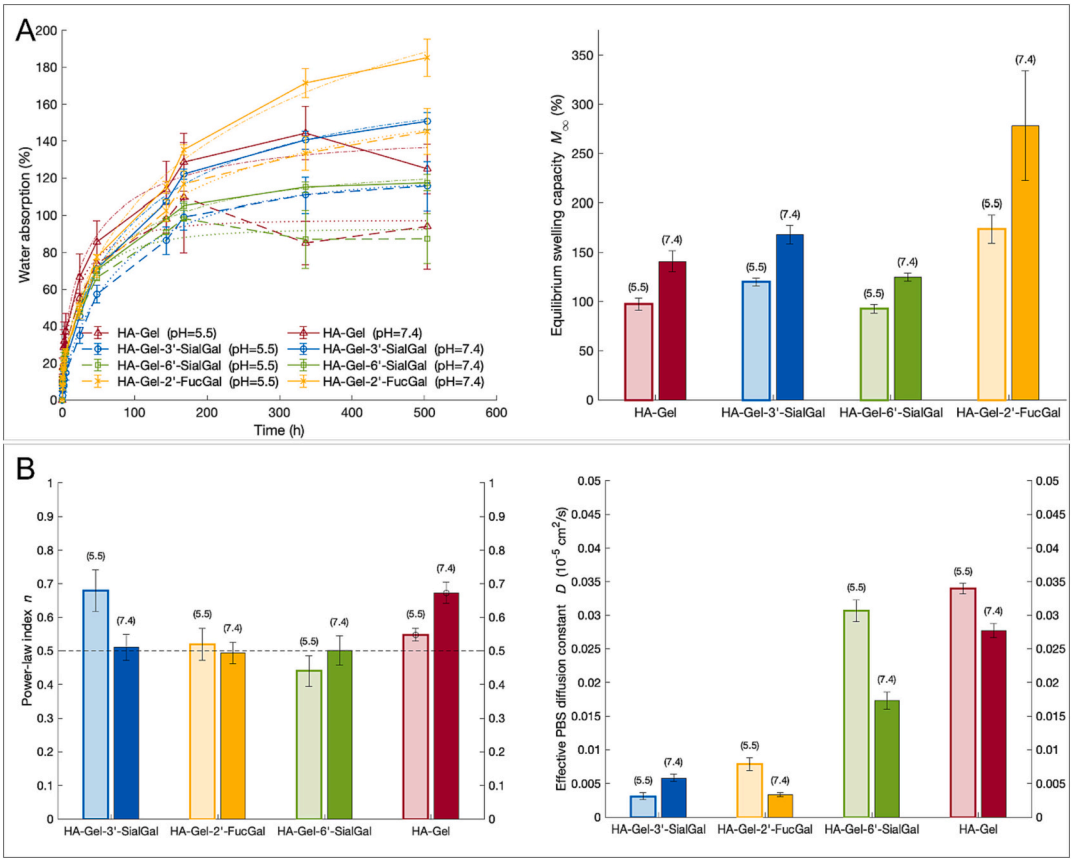

Fig. 5. A Left: data on PBS absorption (mean ± S.D., connected by continuous lines for pH = 7.4 and dashed lines for pH = 5.5) at different times; data are compared with the best fitting curves obtained from Eq. (2) (dotted lines for pH = 5.5 and dot-dashed lines for pH = 7.4). A Right: best-fitting equilibrium swelling capacity M_∞. B Left: power-law index n (the dashed line denotes the value corresponding to a Fickian diffusion mechanism). B Right: effective PBS diffusion coefficient D. The error bars indicate the 75 % confidence interval.

FucGal maintain a Fickian behaviour in the investigated range of pH, revealing themselves to have a robust response upon variations of external conditions. Finally, HA-Gel-3′-SialGal shows an opposite trend, with non-Fickian transport at pH = 5.5 and Fickian diffusion at pH = 7.4. Fig. 5B shows also the obtained diffusion coefficients of PBS. Remarkably, the obtained values are comparable with ranges previously reported for PBS diffusion in gelatin-based gels (0.01–0.03•10^{-5} cm^2/s, see (Chen, Huang, & Ravi-Chandar, 2020; Kripotou et al., 2019; Mel'nichenko et al., 1993). In hydrogels, diffusion coefficients are generally higher at low pH (pH 5.5) than at high pH (pH 7.4), which can be explained by the compaction of the polymer network and/or higher electrostatic interactions at low pH. In fact, HA-Gel-6′-SialGal and HA-Gel-2′-FucGal present high sensitivity to pH, with a halved diffusion coefficient from pH 5.5 to pH 7.4. On the other hand, HA-Gel-3′-SialGal presents an opposite behaviour, that is a diffusion coefficient slightly increasing with pH, confirming the anomalous trend observed also for non-Fickian and Fickian transport mechanisms.

Combining the outcomes of swelling capacity in Fig. 5A with those on diffusivity in Fig. 5B, it is possible to conclude that, although HA-Gel-3′-SialGal and HA-Gel-6′-SialGal present comparable space for water absorption, the diffusion in PBS is significantly faster for HA-Gel-6′-SialGal than for HA-Gel-3′-SialGal. In other words, the "tortuosity" of diffusion paths is higher in HA-Gel-3′-SialGal than in HA-Gel-6′-SialGal. On the other hand, the diffusion coefficient of HA-Gel-2′-FucGal is analogous to that of HA-Gel-3′-SialGal (hence presenting a high "tortuosity pattern"), although this functionalization is characterized by the highest swelling capacity among those tested.

3.5. Degradation test

HA-Gel and HA-Gel-6′SialGal were characterized with a degradation test using hyaluronidase. The weight loss of each sample was calculated at various time intervals. HA-Gel-6′-SialGal showed higher resistance against hyaluronidase compared to HA-Gel. Indeed it takes longer to degrade, indicating lower accessibility in the enzyme active site (SI Fig. 5) (Kurisawa et al., 2005; Le Thi et al., 2020).

3.6. Rheological analysis

The glyco-hydrogels and the control were characterized by a rheological test to evaluate the viscosity curve, the amplitude sweep and frequency sweep. The viscosity of the hydrogels was plot vs. the share rate and the hydrogels show non-Newtonian viscosity behaviour (Fig. 6a). In fact, they exhibit viscosity dependence upon the applied shear conditions, where viscosity decreases with increasing shear rate. No substantial differences are observed among the four hydrogels.

Amplitude sweep test (Fig. 6b) was performed to determine the linear viscoelastic region (LVER), which is the region where the applied stresses are insufficient to cause structural breakdown of the structure. The samples' structure is maintained between 0.1 % and 100 %, so the complex modulus is constant. When the applied stress becomes too high, beyond 100 %, the decomposition of the internal structure occurs, and the modulus changes. The amplitude sweeps of the hydrogels also showed that all of them had a $G'/G'' >> 1$, typical of stronger hydrogels and with modulus <1 kPa, which is suitable for bioprinting purposes according to the literature (Cooke & Rosenzweig, 2021; Liliang et al., 2022; Schwab et al., 2020). In the frequency sweep test (Fig. 6c), in all

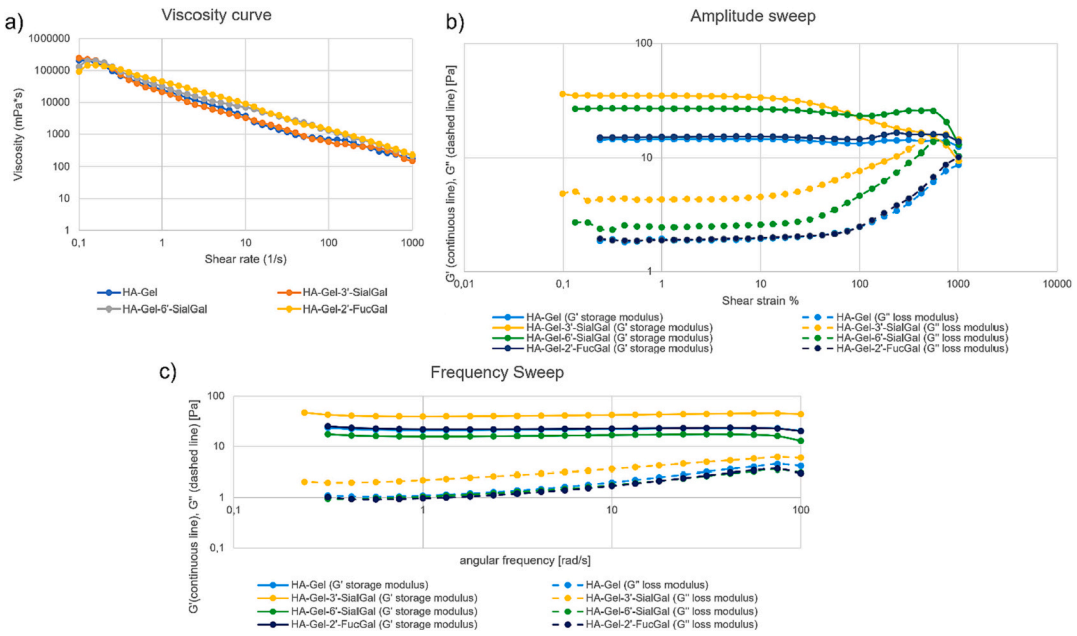

Fig. 6. Rheological test: a) viscosity curve, b) amplitude sweep, c) frequency sweep of glyco-conjugate hydrogels.

hydrogels the elastic modulus values G′ and the viscous modulus values G″ exhibits a pronounced plateau in the frequency range investigated. Also, G′ values are superior to the G″, confirming that the hydrogels have a predominantly gel-like behaviour more solid than liquid.

3.7. Scanning electron microscopy

Hydrogels without cells were analyzed with Scanning electron microscopy (Fig. 7). Images of HA-Gel-6′-SialGal and HA-Gel-3′-SialGal are comparable and result quite different from the control sample, which shows a porous structure. HA-Gel-2′-FucGal appears more similar to the control sample, however bigger porous result in the matrix, in agreement with the evidence that this functionalization shows the highest swelling capacity (see Section 3.4). The morphology of the sialylated samples looks similar to that of human in vivo colon ECM (Almeida et al., 2017), in which big porous are absent. This morphology can be explained considering that both 6′-sialylgalactose and 3′-sialylgalactose present a negatively charged carboxylate at physiological conditions (Alihosseini, 2016; Varki, 2008) that generates ionic interaction with the ammonium ions in gelatin, therefore developing a more compact structure.

3.8. Synchrotron radiation SAXS/WAXS results

Hydrogels were investigated at sub and supramolecular scales by Wide (WAXS) and Small Angle X-ray Scattering (SAXS) microscopies respectively. As shown in Fig. 8 (a), WAXS investigations indicate the presence of the typical collagen's diffraction profile in Gelatine type A (blue profile). Three characteristic peaks were identified: the equatorial peak at q = 0.48 $Å^{-1}$/d = 13.08 Å (marked with blue dash line), related to the lateral packing of collagen, the meridional peak at q = 2.12 $Å^{-1}$/d = 2.96 Å indicating the axial periodicity along the central axis (distance between two adjacent amino acids along the molecular axis), and the wide and broad peak between them at about q = 1.35 $Å^{-1}$/d = 4.65 Å, marker of the amorphous component of collagen (Terzi et al., 2018, 2019). Conversely, only equatorial and amorphous peaks, in the small and wide angle ranges respectively, were identified in the biomaterials. As shown in Fig. 8 (a), a peak shift towards lowest q value (marked with black dash line) was observed in all biomaterials. For a better evaluation of this shift, in Fig. 8 (b) a zoom of the equatorial peak is shown. The blue dash line at q = 0.48 $Å^{-1}$/d = 13.08 Å in Fig. 8 (b) indicates the q value of the equatorial diffraction peak of gelatin powder whose profile (blue) is only shown in Fig. 8 (a). In the range of q values around the equatorial peak, it is possible to clearly observe the peak shift towards lower q value (marked with black dash line), in all the biomaterials except for

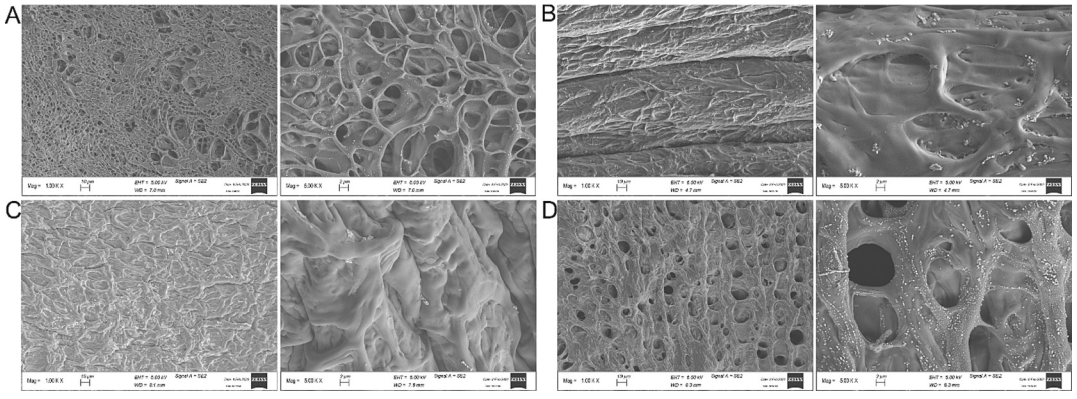

Fig. 7. SEM images of hydrogels: A) HA-Gel, B) HA-Gel-3′-SialGal, C) HA-Gel-6′-SialGal and D) HA-Gel-2′-FucGal.

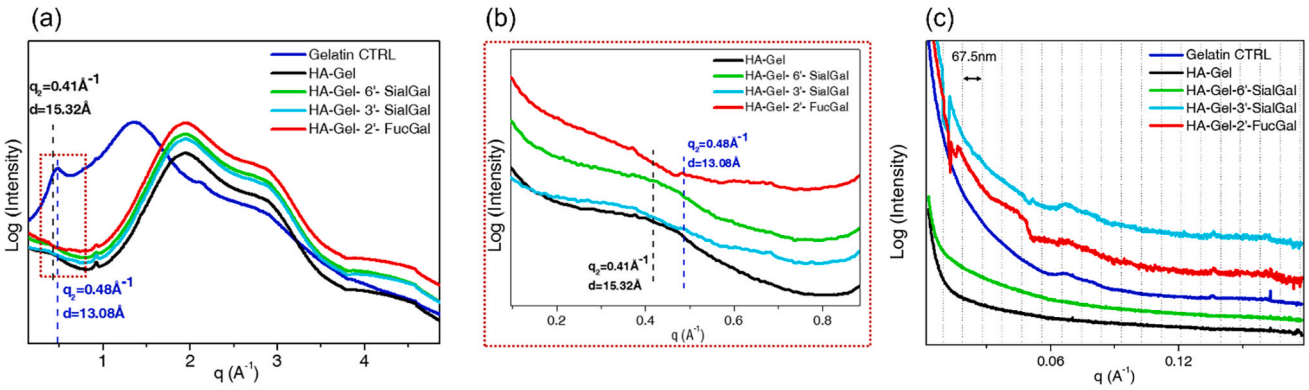

Fig. 8. 1D WAXS profiles of functionalized tissues and gelatin (a) and close-up in the selected q range of the equatorial diffraction peak (b); 1D SAXS profiles of functionalized tissues and gelatin (c).

HA-Gel-2′-FucGal (red profile), in which the peak is not clearly visible indicating a wider lateral distance between collagen molecules in the biomaterials. The shift can be ascribed to both hydration and expansion of the material along the lateral packing direction due to the insertion of sugars, being such expansion effect observed also in sugar insertion within collagen during non-enzymatic glycation (Giannini et al., 2021).

Furthermore, a shift of the amorphous band to higher q values was also observed: from q = 1.35 $Å^{-1}$ / d = 4.65 Å in the gelatin powder A to q = 1.92 $Å^{-1}$/d = 3.27 Å in the biomaterials, indicating a different structure of the biomaterial amorphous component. SAXS measurements were also performed to study the supramolecular fibrillar structure. As shown in Fig. 8 (c), it has been observed that at the nanoscale, gelatin powder (blue), HA-Gel-2′-FucGal (red) and HA-Gel-3′-SialGal (cyan) exhibit a partial maintenance of the collagen structure whose expected periodic distribution of electron density along the fibril axis is marked by the vertical dotted lines (Terzi et al., 2020). It is noteworthy that HA-Gel-2′-FucGal and HA-Gel-3′-SialGal also exhibited the lowest diffusion coefficients in Fig. 5B, revealing a correlation between the existence of a supramolecular structure and an increase of "tortuosity paths" hindering diffusion. Finally, it is worth remembering that HA-Gel-2′-FucGal is the one without visible molecular structure which is instead present in all other biomaterials. Therefore, as shown in Table 2, the hierarchical arrangement at *both* atomic and nanoscale, apart from gelatin powder, is present only in one functionalized biomaterial, that is HA-Gel-3′-SialGal.

3.9. In vitro cytotoxicity

The vitality of HT29 cells inside the hydrogels was tested by Live/Dead assay at 1, 3 and 7 days (Fig. 7 SI). After 7 days, interestingly, an increase of cells viability was observed, as shown by the more intense green fluorescence. Furthermore, a cluster organization of the cells inside the hydrogel is clearly visible, which indicates proliferation capacity. The hydrogel therefore resulted not cytotoxic and suitable for maintain the cells vitality and proliferation.

3.10. Morphological analysis of 3D bioprinted HT29

Cells morphologies inside the 3D hydrogel were examined using Phalloidin to highlight the cytoskeleton and DAPI to visualize the nuclei (Fig. 9). Firstly, HT29 cells line were selected as model and encapsulated in the four different hydrogels. After 14 days the cells were organized in clusters with an average diameter of 70 μm for HA-Gel-2′-FucGal, 64 μm for HA-Gel-3′-SialGal, 77 μm for HA-Gel-6′-SialGal and 84 μm for HA-Gel. The clusters dimensions are comparable with those of CRC patient derived organoids reported in literature (Luo et al., 2021) and with other models of HT29 cultured in 3D for 14 days (Magdeldin et al., 2014). In terms of shape and distribution, the clusters of the control sample (HA-Gel) are round and isolated, while in the glyco-hydrogels HA-Gel-6′-SialGal and HA-Gel-3′-SialGal the clusters are smaller, slightly elongated and closer to each other. This behaviour can explain the tendency to migrate and metastatize, observed in CRC with aberrant 6-sialyllation (Park & Lee, 2013). Interestingly, in HA-Gel-2′-FucGal the clusters are numerous, as in the sialyl-hydrogel, but present a shape and a porous structure more similar to the control HA-Gel. The larger porous structure of the hydrogel can facilitate the growth of circular bigger cluster (Fan & Wang, 2015).

Table 2
Multilevel hierarchical arrangement of the samples.

Samples	Molecular structure	Supramolecular structure
Gel CTRL	✓	✓
HA-Gel	✓	
HA-Gel-6′-SialGal	✓	
HA-Gel-3′-SialGal	✓	✓
HA - Gel-2′-FucGal		✓

3.11. MALDI-MS imaging analysis

The protein profiles of the cells cultured in the differently glycosylated hydrogels were analyzed by MALDI-MS. Initially, the segmentation tree was expanded in order to highlight the spectral clusters which followed the cellular structures present within each 3D hydrogel tumoroid. These spectra were then used to generate the average protein profiles of the produced cells (SI Fig. 6). Notably, the various matrices induced alterations to the cluster cell proteomes, with each sample having its own distinct cloud within the PCA score chart differing from control (HA-Gel) (Fig. 10, top). Interestingly, the protein profiles of cells produced by the HA-Gel-3′-SialGal (maroon) and HA-Gel-6′-SialGal (orange) matrices were most similar to one another and most different to those produced by HA-Gel-2′-FucGal (blue), indicating that sialylation and fucosylation of ECM proteins may induce diverse alterations to the proteome of the cluster and surrounding cells (West et al., 2018). This is also highlighted by a protein feature (at *m/z* 1184.6) whose distribution closely follows the border of the cluster structures and is of higher relative abundance (AUC >0.8) in those cells produced by the HA-Gel-3′-SialGal (maroon) and HA-Gel-6′-SialGal (orange) ECM with respect to HA-Gel-2′-FucGal (blue) and HA-Gel (green) (Fig. 10, bottom).

3.12. 3D bioprinting of CRC patient derived tumoroids

Tumoroids from CRC patients cultured in 3D hydrogels (HA-Gel-6′SialGal and HA-Gel) were examined using Phalloidin to highlight the cytoskeleton and DAPI to visualize nuclei (SI Fig. 8). After 21 days the tumoroids were efficiently grown and single cells were detected also outside the tumoroid structures, indicating a certain level of cells

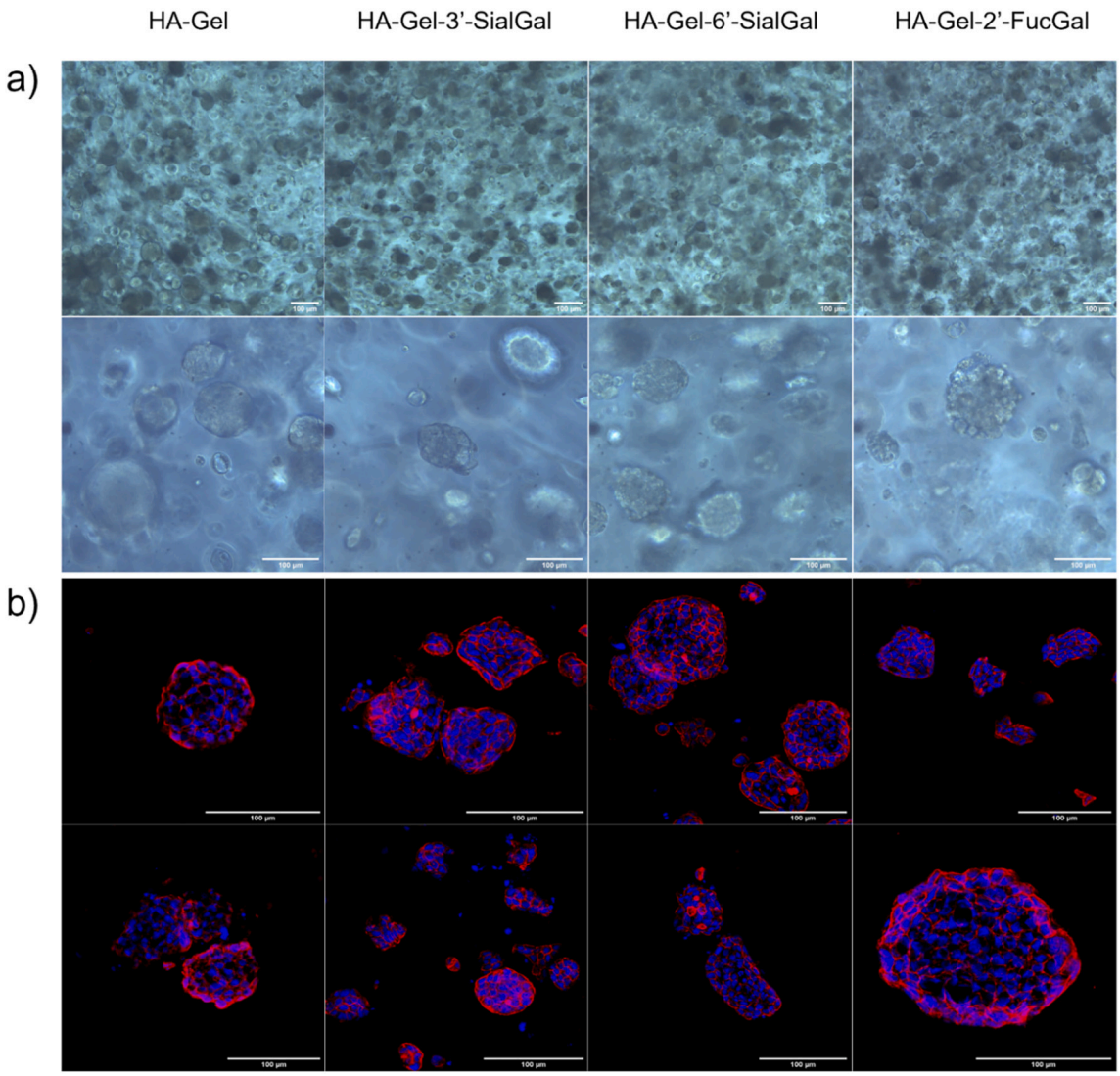

Fig. 9. a) Optical images of 3D bioprinted hydrogels after 14 days of 3D cell culture; b) confocal images of hydrogels after 14 days of 3D cell culture. Scale bar 100 μm.

motility. Notably, in HA-Gel-6′-SialGal tumoroids were present in higher number and maintained their original structure as compared to control (HA-Gel). Moreover, in the HA-Gel-6′-SialGal matrix, a higher number of single cells outside the tumoroids were detected, indicating a higher ability to migrate outside the original structure, which could be related to the higher diffusion coefficient (Paragraph 3.4) (Hadden et al., 2017; Marel et al., 2014). Notably, this aspect is quite important as single cell can lead to the formation of a new tumoroid. The higher proliferation in HA-Gel-6′-SialGal is evident also with H&E staining reported in Fig. 11. Moreover, in the light of our observation that differential glycosylation of collagen modulates lung cancer stem cell subsets through β1 integrin-mediated interactions (Gardelli et al., 2021), we tested the tumoroids from CRC patients in HA-Gel-6′-SialGal and HA-Gel as control with markers CD133 (Dobie & Skropeta, 2020; Y. Wu & Wu, 2009) and LGR5 (Morgan et al., 2018; X. S. Wu et al., 2012) (SI Fig. 9). CD133 is a transmembrane glycoprotein present in embryonic epithelial structures and hematopoietic stem cells (Talukdar et al., 2016; Yin et al., 1997) and is considered a cancer stem cells (CSC) marker in different solid tumor including colon (Botchkina, 2013). LGR5 in normal intestinal homeostasis marks the stem cells located at the crypt base, however its expression is detected also in CRC progression (Espersen et al., 2015) in particular a higher expression was detected in the invasive front of the tumors and in metastases (Baker et al., 2015; Gao et al., 2014; He et al., 2014; Wu et al., 2012). In our experiment, tumoroids cultured in HA-Gel-6′-SialGal showed a higher expression of CD133 and LGR5 compared to the control, indicating that 6′-SialGal in ECM induces a modulation of stemness phenotype in CRC. Moreover, in HA-Gel-6′SialGal a higher number of single cells outside the tumoroids were observed and some of them resulted positive to LGR5 which can confirm the correlation with cancer migration and metastases.

4. Conclusion

This study underlines the importance of the glycosignature in the development of 3D bioprinted tissue models and describes a protocol to generate glycosylated hydrogels suitable for 3D bioprinting. The obtained hydrogels resulted biocompatible and stable over the time for 3D culture both with HT29 and patient derived CRC tumoroids. The functionalization with glycans induces structural modifications of the final 3D construct, as demonstrated with SAXS/WAXS and swelling analysis, and influences the cell fate as shown also by the cell proteomes obtained by MALDI-MS analysis. Indeed, sialylated hydrogels, HA-Gel-3′-SialGal and HA-Gel-6′-SialGal, induce significant and comparable alterations in cell proteome with respect to the control, whereas the cell protein profiles in HA-Gel-2′-FucGal is significantly different. This is a further confirmation that different glycosylations of cell microenvironment,

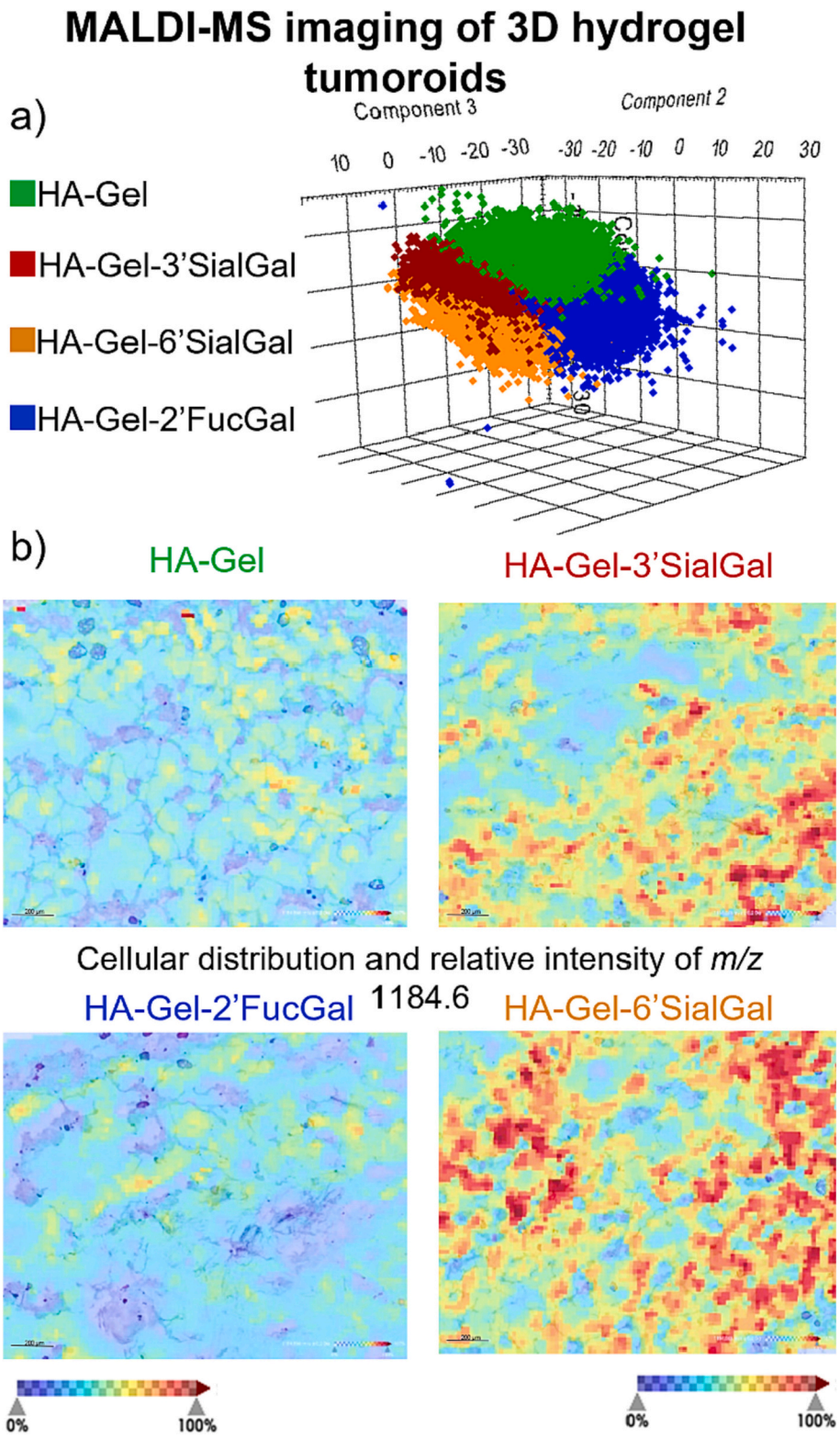

Fig. 10. a) 3D principal component analyses score chart using tumor cell protein profiles produced by each glycosylation condition, with each coloured dot representing an individual protein profile (mass spectrum); control (Green), HA-Gel-3′SialGal (maroon), HA-Gel-6′SialGal (orange), and HA-Gel-2′FucGal (blue). b) Example MALDI-MS image highlighting the distribution and relative intensity of m/z 1184.6 in the cellular regions of 3D hydrogel tumoroids produced by each glycosylation condition. The H&E image of each hydrogel tumoroid has been overlaid with the MALDI-MS image to highlight the presence of cells (transparent purple regions). An intensity scale bar is also provided to indicate the relative intensity of the protein signal, with dark blue representing a low intensity (0 %) and dark red representing a high intensity (100 %).

more specifically sialylation and fucosylation, induce diverse alterations of the tumoroid and surrounding cells. It is possible to hypothesize a correlation between change in matrix morphology and modification of cell line proteome induced by the different ECM glycosylation. Indeed HA-Gel-3′-SialGal and HA-Gel-6′-SialGal presented similar porosity and similar cell protein profiles, totally different with respect to HA-Gel-2′-FucGal. It is therefore of fundamental importance to develop efficient protocols to generate properly glycosylated 3D tissue models in order to better understand the impact of ECM glycosylation in cell face and to develop artificial 3D tissues for animal free personalized drug testing.

Ethics statement

Study approved by the local Ethical Committee (Comitato Etico,

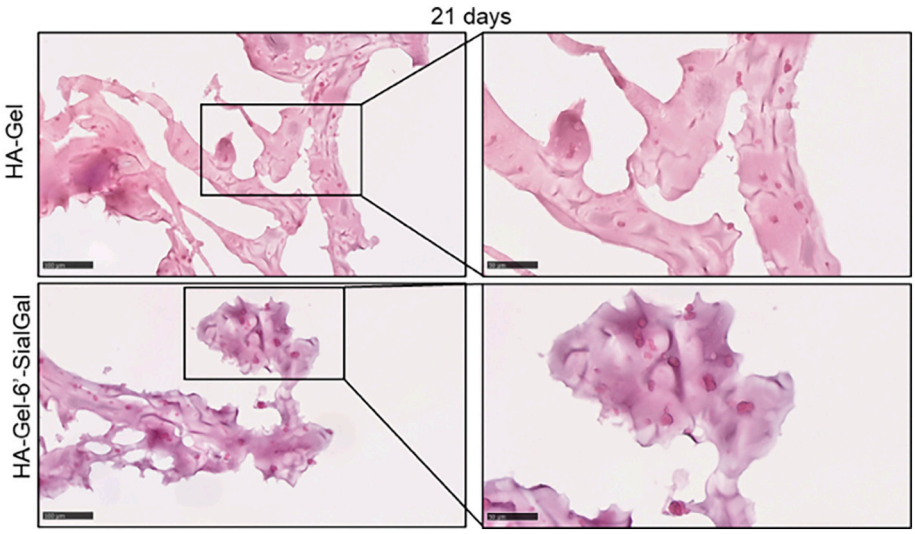

Fig. 11. H&E staining of slices of 3D bioprinted construct with tumoroids after 21 days. Scale bar 100 μm.

UNIMIB, Italy), Cod. TUM-DC/349 (10/12/2020), written informed consent was obtained from all patients and healthy subjects before they entered the study, performed in accordance with the Declaration of Helsinki.

CRediT authorship contribution statement

Francesca Cadamuro (investigation, methodology, validation, writing, editing), **Laura Marongiu** (investigation tumoroids, writing), **Michele Marino** (writing, investigation, methodology, editing), **Nicolò Tamini** (resources tumoroids), **Luca Nespoli** (resources tumoroids), **Nicola Zucchini** (resources tumoroids), **Alberta Terzi** (investigation SAXS/WAXS, writing, editing), **Davide Altamura** (investigation SAXS/WAXS), **Zirui Gao** (investigation SAXS/WAXS), **Cinzia Giannini** (investigation SAXS/WAXS, writing, editing), **Greta Bindi** (investigation MS), **Andrew Smith** (investigation MS, writing), **Fulvio Magni** (resources MS), **Sabrina Bertini** (resources reology), **Francesca Granucci** (resources tumoroids), **Francesco Nicotra** (funding acquisition, writing, editing), **Laura Russo** (conceptualization, supervision, project administration, writing, editing).

Declaration of competing interest

The authors declare that they have no known competing financial interests or personal relationships that could have appeared to influence the work reported in this paper.

Data availability

Data will be made available on request.

Acknowledgements

The authors acknowledge funding from: Italian Ministry of Health (Grant No. RF-2016- 02362946); POR-FESR 2014-2020, Innovazione e Competitività, and Progetti Strategici di Ricerca, Sviluppo e Innovazione, IMMUN-HUB; EC, H2020-NMBP-15-2017-GA-760986, (iNanoBIT); SNSF, project number 200021_178788; MIUR PRIN2017, SAPIENT" 2017CBHCWF; Regione Lazio (POR FESR LAZIO 2014; Progetti di Gruppi di Ricerca 2020; project: BIOPMEAT, n. A0375-2020-36756).

Access to the cSAXS beamline of the Swiss Light Source at the Paul Scherrer Institute has been supported by the EU H2020 GA No. 731019 (EUSMI; to C.Giannini), proposal no. E190400272. We gratefully acknowledge support by Andreas Menzel during that beam time, further technical support by Xavier Donath and Mirko Holler, post-experiment data analysis support and fruitful discussions by Oliver Bunk.

Appendix A. Supplementary data

Supplementary data to this article can be found online at https://doi.org/10.1016/j.carbpol.2022.120395.

References

Alheib, O., Da Silva, L. P., Youn, Y. H., Kwon, I. K., Reis, R. L., & Correlo, V. M. (2021). 3D bioprinting: A step forward in creating engineered human tissues and organs. *Additive Manufacturing*, 599–633. https://doi.org/10.1016/B978-0-12-818411-0.00016-1

Alihosseini, F. (2016). Plant-based compounds for antimicrobial textiles. *Antimicrobial Textiles*, 155–195. https://doi.org/10.1016/B978-0-08-100576-7.00010-9

Almeida, L. D., Quaglio, A. E. V., De Almeida Costa, C. A. R., & Di Stasi, L. C. (2017). Intestinal anti-inflammatory activity of Ground Cherry (Physalis angulata L.) standardized CO_2 phytopharmaceutical preparation. *World Journal of Gastroenterology, 23*(24), 4369–4380. https://doi.org/10.3748/WJG.V23.I24.4369

Amorim, S., Reis, C. A., Reis, R. L., & Pires, R. A. (2021). Extracellular matrix mimics using hyaluronan-based biomaterials. *Trends in Biotechnology, 39*(1), 90–104. https://doi.org/10.1016/j.tibtech.2020.06.003

Baker, A. M., Graham, T. A., Elia, G., Wright, N. A., & Rodriguez-Justo, M. (2015). Characterization of LGR5 stem cells in colorectal adenomas and carcinomas. *Scientific Reports, 5*(1), 1–8. https://doi.org/10.1038/srep08654

Botchkina, G. (2013). Colon cancer stem cells – From basic to clinical application. *Cancer Letters, 338*(1), 127–140. https://doi.org/10.1016/J.CANLET.2012.04.006

Boyaval, F., Ren, R., Van Zeijl, R., Dalebout, H., Holst, S., Van Pelt, G., Fariña-Sarasqueta, A., Mesker, W., Tollenaar, R., Morreau, H., Wuhrer, M., & Heijs, B. (2021). N-glycomic signature of stage ii colorectal cancer and its association with the tumor microenvironment. *Molecular & Cellular Proteomics, 20*, 100057. https://doi.org/10.1074/mcp.RA120.002215

Bunk, O., Bech, M., Jensen, T. H., Feidenhans'L, R., Binderup, T., Menzel, A., & Pfeiffer, F. (2009). Multimodal x-ray scatter imaging. *New Journal of Physics, 11*(12), 123016. https://doi.org/10.1088/1367-2630/11/12/123016

Burkholder-Wenger, A. C., Golzar, H., Wu, Y., & Tang, X. S. (2022). Development of a Hybrid Nanoink for 3D Bioprinting of Heterogeneous Tumor Models. *ACS Biomaterials Science & Engineering, 8*(2), 777–785. https://doi.org/10.1021/ACSBIOMATERIALS.1C01265/SUPPL_FILE/AB1C01265_SI_001.PDF

Chen, H., Cheng, Y., Wang, X., Wang, J., Shi, X., Li, X., Tan, W., & Tan, Z. (2020). 3D printed in vitro tumor tissue model of colorectal cancer. *Theranostics, 10*(26), 12127. https://doi.org/10.7150/THNO.52450

Chen, S., Huang, R., & Ravi-Chandar, K. (2020). Linear and nonlinear poroelastic analysis of swelling and drying behavior of gelatin-based hydrogels. *International Journal of Solids and Structures, 195*, 43–56. https://doi.org/10.1016/J.IJSOLSTR.2020.03.017

Chen, Y., Xu, L., Li, W., Chen, W., He, Q., Zhang, X., Tang, J., Wang, Y., Liu, B., & Liu, J. (2022). 3D bioprinted tumor model with extracellular matrix enhanced bioinks for nanoparticle evaluation. *Biofabrication, 14*(2), Article 025002. https://doi.org/10.1088/1758-5090/AC48E4

Cooke, M. E., & Rosenzweig, D. H. (2021). The rheology of direct and suspended extrusion bioprinting. *APL Bioengineering, 5*(1), Article 011502. https://doi.org/10.1063/5.0031475

Davidenko, N., Schuster, C. F., Bax, D. V., Farndale, R. W., Hamaia, S., Best, S. M., & Cameron, R. E. (2016). Evaluation of cell binding to collagen and gelatin: a study of theeffect of 2D and 3D architecture and surface chemistry. *Journal of Materials Science: Materials in Medicine, 27*(10), 148. https://doi.org/10.1007/S10856-016-5763-9

Dobie, C., & Skropeta, D. (2020). Insights into the role of sialylation in cancer progression and metastasis. *British Journal of Cancer, 124*(1), 76–90. https://doi.org/10.1038/s41416-020-01126-7

Espersen, M. L. M., Olsen, J., Linnemann, D., Høgdall, E., & Troelsen, J. T. (2015). Clinical Implications of Intestinal Stem Cell Markers in Colorectal Cancer. *Clinical Colorectal Cancer, 14*(2), 63–71. https://doi.org/10.1016/J.CLCC.2014.12.004

Fan, C., & Wang, D. A. (2015). Effects of permeability and living space on cell fate and neo-tissue development in hydrogel-based scaffolds: A study with cartilaginous model. *Macromolecular Bioscience, 15*(4), 535–545. https://doi.org/10.1002/MABI.201400453

Gao, F. J., Chen, J. Y., Wu, H. Y., Shi, J., Chen, M., Fan, X. S., & Huang, Q. (2014). Lgr5 over-expression is positively related to the tumor progression and HER2 expression in stage pTNM IV colorectal cancer. *International Journal of Clinical and Experimental Pathology, 7*(4), 1572. PMC4014237.

Gardelli, C., Russo, L., Cipolla, L., Moro, M., Andriani, F., Rondinone, O., Nicotra, F., Sozzi, G., Bertolini, G., & Roz, L. (2021). Differential glycosylation of collagen modulates lung cancer stem cell subsets through β1 integrin-mediated interactions. *Cancer Science, 112*(1), 217–230. https://doi.org/10.1111/cas.14700

Giannini, C., De Caro, L., Terzi, A., Fusaro, L., Altamura, D., Diaz, A., Lassandro, R., Boccafoschi, F., & Bunk, O. (2021). Decellularized pericardium tissues at increasing glucose, galactose and ribose concentrations and at different time points studied using scanning X-ray microscopy. *IUCrJ, 8*(4), 621–632. https://doi.org/10.1107/S2052252521005054/RO5026SUP1.PDF

Giussani, M., Triulzi, T., Sozzi, G., & Tagliabue, E. (2019). Tumor extracellular matrix remodeling: new perspectives as a circulating tool in the diagnosis and prognosis of solid tumors. *Cells, 8*(*2*), *81*. https://doi.org/10.3390/CELLS8020081

Hadden, W. J., Young, J. L., Holle, A. W., McFetridge, M. L., Kim, D. Y., Wijesinghe, P., … Cho, Y. S. (2017). Stem cell migration and mechanotransduction on linear stiffness gradient hydrogels. *Proceedings of the National Academy of Sciences of the United States of America, 114*(22), 5647–5652. https://doi.org/10.1073/PNAS.1618239114/SUPPL_FILE/PNAS.1618239114.SM11.AVI

Han, H., Park, Y., Choi, Y.m., Yong, U., Kang, B., Shin, W., … Jang, J. (2022). A bioprinted tubular intestine model using a colon-specific extracellular matrix bioink. *Advanced Healthcare Materials, 11*(2). https://doi.org/10.1002/ADHM.202101768

He, S., Zhou, H., Zhu, X., Hu, S., Fei, M., Wan, D., Gu, W., Yang, X., Shi, D., Zhou, J., Zhou, J., Zhu, Z., Wang, L., Li, D., & Zhang, Y. (2014). Expression of Lgr5, a marker of intestinal stem cells, in colorectal cancer and its clinicopathological significance. *Biomedicine & Pharmacotherapy, 68*(5), 507–513. https://doi.org/10.1016/J.BIOPHA.2014.03.016

Jung, M., Skhinas, J. N., Du, E. Y., Tolentino, M. A. K., Utama, R. H., Engel, M., … Kavallaris, M. (2021). A high-throughput 3D bioprinted cancer cell migration and invasion model with versatile and broad biological applicability. *BioRxiv, 2021*(12), 28.474387. https://doi.org/10.1101/2021.12.28.474387

Kačarević, Ž. P., Rider, P. M., Alkildani, S., Retnasingh, S., Smeets, R., Jung, O., … Barbeck, M. (2018). An Introduction to 3D bioprinting: possibilities, challenges and future aspects. *Materials, 11*(11). https://doi.org/10.3390/MA11112199

Kawai, S., Yamazaki, M., Shibuya, K., Yamazaki, M., Fujii, E., Nakano, K., & Suzuki, M. (2020). Three-dimensional culture models mimic colon cancer heterogeneity induced by different microenvironments. *Scientific Reports, 10*(1), 1–11. https://doi.org/10.1038/s41598-020-60145-9

Kripotou, S., Stefanopoulou, E., Culebras-Martínez, M., Morales-Román, R. M., Gallego Ferrer, G., & Kyritsis, A. (2019). Water dynamics and thermal properties of tyramine-modified hyaluronic acid - Gelatin hydrogels. *Polymer*, 178. https://doi.org/10.1016/J.POLYMER.2019.121598

Kurisawa, M., Chung, J. E., Yang, Y. Y., Gao, S. J., & Uyama, H. (2005). Injectable biodegradable hydrogels composed of hyaluronic acid-tyramine conjugates for drug delivery and tissue engineering. *Chemical Communications (Cambridge, England), 34*, 4312–4314. https://doi.org/10.1039/B506989K

Langer, E. M., Allen-Petersen, B. L., King, S. M., Kendsersky, N. D., Turnidge, M. A., Kuziel, G. M., … Sears, R. C. (2019). Modeling Tumor Phenotypes In Vitro with Three-Dimensional Bioprinting. *Cell Reports, 26*(3), 608–623. e6 https://doi.org/10.1016/J.CELREP.2018.12.090.

Le Thi, P., Son, J. Y., Lee, Y., Ryu, S. B., Park, K. M., & Park, K. D. (2020). Enzymatically crosslinkable hyaluronic acid-gelatin hybrid hydrogels as potential bioinks for tissue regeneration. *Macromolecular Research, 28*(4), 400–406. https://doi.org/10.1007/S13233-020-8052-X

Levato, R., Jungst, T., Scheuring, R. G., Blunk, T., Groll, J., & Malda, J. (2020). From shape to function: the next step in bioprinting. *Advanced Materials, 32*(12), 1906423. https://doi.org/10.1002/adma.201906423

Li, F., & Ding, J. (2019). Sialylation is involved in cell fate decision during development, reprogramming and cancer progression. *Protein & Cell, 10*(8), 550–565. https://doi.org/10.1007/S13238-018-0597-5/FIGURES/5

Liliang, O., K, A. J. P., Yiyang, L., P, W. J., Charlotte, L.-R., Daniel, H., … M, S. M. (2022). Expanding and optimizing 3D bioprinting capabilities using complementary network bioinks. *Science Advances, 6*(38), eabc5529. https://doi.org/10.1126/sciadv.abc5529

Lugli, A., Zlobec, I., Günthert, U., Minoo, P., Baker, K., Tornillo, L., … Jass, J. R. (2006). Overexpression of the receptor for hyaluronic acid mediated motility is an independent adverse prognostic factor in colorectal cancer. *Modern Pathology, 19*(10), 1302–1309. https://doi.org/10.1038/modpathol.3800648

Luo, X., Fong, E. L. S., Zhu, C., Lin, Q. X. X., Xiong, M., Li, A., … Liu, S. (2021). Hydrogel-based colorectal cancer organoid co-culture models. *Acta Biomaterialia, 132*, 461–472. https://doi.org/10.1016/J.ACTBIO.2020.12.037

Lutz-Bueno, V., Arboleda, C., Leu, L., Blunt, M. J., Busch, A., Georgiadis, A., … Menzel, A. (2018). Model-free classification of X-ray scattering signals applied to image segmentation. *Urn:Issn:1600-5767, 51*(5), 1378–1386. https://doi.org/10.1107/S1600576718011032

Magalhães, A., Duarte, H. O., & Reis, C. A. (2017). Aberrant glycosylation in cancer: a novel molecular mechanism controlling metastasis. *Cancer Cell, 31*(6), 733–735. https://doi.org/10.1016/J.CCELL.2017.05.012

Magdeldin, T., López-Dávila, V., Villemant, C., Cameron, G., Drake, R., Cheema, U., & Loizidou, M. (2014). The efficacy of cetuximab in a tissue-engineered three-dimensional in vitro model of colorectal cancer. *Journal of Tissue Engineering, 5*. https://doi.org/10.1177/2041731414544183

Magli, S., Rossi, L., Consentino, C., Bertini, S., Nicotra, F., & Russo, L. (2021). Combined Analytical Approaches to Standardize and Characterize Biomaterials Formulations: Application to Chitosan-Gelatin Cross-Linked Hydrogels. *Biomolecules, 11*(5), 683. https://doi.org/10.3390/BIOM11050683

Marel, A. K., Zorn, M., Klingner, C., Wedlich-Söldner, R., Frey, E., & Rädler, J. O. (2014). Flow and diffusion in channel-guided cell migration. *Biophysical Journal, 107*(5), 1054. https://doi.org/10.1016/J.BPJ.2014.07.017

Mel'nichenko, Y. B., Klepko, V. V., & Shilov, V. V. (1993). Self-diffusion of water in gelatin gels: 1. Macroscopic measurements by tracer technique. *Polymer, 34*(5), 1019–1023. https://doi.org/10.1016/0032-3861(93)90223-W

Morgan, R. G., Mortensson, E., & Williams, A. C. (2018). Targeting LGR5 in Colorectal Cancer: therapeutic gold or too plastic? *British Journal of Cancer, 118*(11), 1410–1418. https://doi.org/10.1038/s41416-018-0118-6

Mota, C., Camarero-Espinosa, S., Baker, M. B., Wieringa, P., & Moroni, L. (2020). Bioprinting: from tissue and organ development to in vitro models. *Chemical Reviews, 120*(19), 10547–10607. https://doi.org/10.1021/ACS.CHEMREV.9B00789

Nicolas, J., Magli, S., Rabbachin, L., Sampaolesi, S., Nicotra, F., & Russo, L. (2020). 3D extracellular matrix mimics: fundamental concepts and role of materials chemistry to influence stem cell fate. *Biomacromolecules, 21*(6), 1968–1994. https://doi.org/10.1021/ACS.BIOMAC.0C00045

Nyga, A., Loizidou, M., Emberton, M., & Cheema, U. (2013). A novel tissue engineered three-dimensional in vitro colorectal cancer model. *Acta Biomaterialia, 9*(8), 7917–7926. https://doi.org/10.1016/J.ACTBIO.2013.04.028

Ouyang, L. (2022). Pushing the rheological and mechanical boundaries of extrusion-based 3D bioprinting. *Trends in Biotechnology, 40*(7), 891–902. https://doi.org/10.1016/J.TIBTECH.2022.01.001

Park, J. J., & Lee, M. (2013). Increasing the α 2, 6 sialylation of glycoproteins may contribute to metastatic spread and therapeutic resistance in colorectal cancer. *Gut and Liver, 7*(6), 629. https://doi.org/10.5009/GNL.2013.7.6.629

Peixoto, A., Relvas-Santos, M., Azevedo, R., Lara Santos, L., & Ferreira, J. A. (2019). Protein glycosylation and tumor microenvironment alterations driving cancer hallmarks. *Frontiers in Oncology, 9*(MAY), 380. https://doi.org/10.3389/FONC.2019.00380/BIBTEX

Pinho, S. S., & Reis, C. A. (2015). Glycosylation in cancer: mechanisms and clinical implications. *Nature Reviews Cancer, 15*(9), 540–555. https://doi.org/10.1038/nrc3982

Rodrigues, J. G., Duarte, H. O., Gomes, C., Balmaña, M., Martins, Á. M., Hensbergen, P. J., … Reis, C. A. (2021). Terminal α2,6-sialylation of epidermal growth factor receptor modulates antibody therapy response of colorectal cancer cells. *Cellular Oncology, 44*(4), 835–850. https://doi.org/10.1007/S13402-021-00606-Z/FIGURES/5

Russo, L., Sgambato, A., Visone, R., Occhetta, P., Moretti, M., Rasponi, M., Nicotra, F., & Cipolla, L. (2016). Gelatin hydrogels via thiol-ene chemistry. *Monatshefte Fur Chemie, 147*(3). https://doi.org/10.1007/s00706-015-1614-5

Sampaolesi, S., Nicotra, F., & Russo, L. (2019). Glycans in nanomedicine, impact and perspectives. *Future Medicinal Chemistry, 11*(1), 43–60. https://doi.org/10.4155/fmc-2018-0368

Sbirkov, Y., Molander, D., Milet, C., Bodurov, I., Atanasov, B., Penkov, R., Belev, N., Forraz, N., McGuckin, C., & Sarafian, V. (2021). A colorectal cancer 3D bioprinting workflow as a platform for disease modeling and chemotherapeutic screening. *Frontiers in Bioengineering and Biotechnology, 9*, 910. https://doi.org/10.3389/FBIOE.2021.755563/BIBTEX

Schwab, A., Levato, R., D'Este, M., Piluso, S., Eglin, D., & Malda, J. (2020). Printability and shape fidelity of bioinks in 3d bioprinting. *Chemical Reviews, 120*(19), 11028–11055. https://doi.org/10.1021/acs.chemrev.0c00084

Sensi, F., D'angelo, E., Piccoli, M., Pavan, P., Mastrotto, F., Caliceti, P., Biccari, A., Corallo, D., Urbani, L., Fassan, M., Spolverato, G., Riello, P., Pucciarelli, S., & Agostini, M. (2020). Recellularized colorectal cancer patient-derived scaffolds as in vitro pre-clinical 3D model for drug screening. *Cancers, 12*(3), 681. https://doi.org/10.3390/CANCERS12030681

Talukdar, S., Emdad, L., Das, S. K., Sarkar, D., & Fisher, P. B. (2016). Evolving strategies for therapeutically targeting cancer stem cells. *Advances in Cancer Research, 131*, 159–191. https://doi.org/10.1016/BS.ACR.2016.04.003

Terzi, A., Storelli, E., Bettini, S., Sibillano, T., Altamura, D., Salvatore, L., Madaghiele, M., Romano, A., Siliqi, D., Ladisa, M., De Caro, L., Quattrini, A., Valli, L., Sannino, A., & Giannini, C. (2018). Effects of processing on structural, mechanical and biological properties of collagen-based substrates for regenerative

medicine. *Scientific Reports, 8*(1), 1–13. https://doi.org/10.1038/s41598-018-19786-0

Terzi, A., Gallo, N., Bettini, S., Sibillano, T., Altamura, D., Campa, L., … Giannini, C. (2019). Investigations of processing–induced structural changes in horse type-i collagen at sub and supramolecular levels. *Frontiers in Bioengineering and Biotechnology, 7*(AUG), 203. https://doi.org/10.3389/FBIOE.2019.00203/BIBTEX

Terzi, A., Gallo, N., Bettini, S., Sibillano, T., Altamura, D., Madaghiele, M., De Caro, L., Valli, L., Salvatore, L., Sannino, A., Giannini, C., Terzi, A., Sibillano, T., Altamura, D., De Caro, L., Giannini, C., Gallo, N., Bettini, S., Madaghiele, M., … Valli, L. (2020). Sub- and supramolecular x-ray characterization of engineered tissues from equine tendon, bovine dermis, and fish skin type-I collagen. *Macromolecular Bioscience, 20*(5), 2000017. https://doi.org/10.1002/MABI.202000017

Varki, A. (2008). Sialic acids in human health and disease. *Trends in Molecular Medicine, 14*(8), 351–360. https://doi.org/10.1016/J.MOLMED.2008.06.002

Venkitachalam, S., Revoredo, L., Varadan, V., Fecteau, R. E., Ravi, L., Lutterbaugh, J., … Guda, K. (2016). Biochemical and functional characterization of glycosylation-associated mutational landscapes in colon cancer. *Scientific Reports, 6*(1), 1–11. https://doi.org/10.1038/srep23642

Wang, D., Madunić, K., Zhang, T., Mayboroda, O. A., Lageveen-Kammeijer, G. S. M., & Wuhrer, M. (2022). High diversity of glycosphingolipid glycans of colorectal cancer cell lines reflects the cellular differentiation phenotype. *Molecular and Cellular Proteomics, 21*(6), 100239. https://doi.org/10.1016/j.mcpro.2022.100239

West, C. A., Wang, M., Herrera, H., Liang, H., Black, A., Angel, P. M., … Mehta, A. S. (2018). N-Linked glycan branching and fucosylation are increased directly in Hcc tissue as determined through in situ glycan imaging. *Journal of Proteome Research, 17*(10), 3454–3462. https://doi.org/10.1021/ACS.JPROTEOME.8B00323/SUPPL_FILE/PR8B00323_SI_001.PDF

Wiig, H., Gyenge, C., Iversen, P. O., Gullberg, D., & Tenstad, O. (2008). The role of the extracellular matrix in tissue distribution of macromolecules in normal and pathological tissues: Potential therapeutic consequences. *Microcirculation, 15*(4), 283–296. https://doi.org/10.1080/10739680701671105

Wu, X. S., Xi, H. Q., & Chen, L. (2012). Lgr5 is a potential marker of colorectal carcinoma stem cells that correlates with patient survival. *World Journal of Surgical Oncology, 10*(1), 1–8. https://doi.org/10.1186/1477-7819-10-244/FIGURES/3

Wu, Y., & Wu, P. Y. (2009). CD133 as a marker for cancer stem cells: progresses and concerns. *Stem Cells and Development, 18*(8), 1127–1134. https://doi.org/10.1089/SCD.2008.0338

Yin, A. H., Miraglia, S., Zanjani, E. D., Almeida-Porada, G., Ogawa, M., Leary, A. G., … Buck, D. W. (1997). AC133, a novel marker for human hematopoietic stem and progenitor cells. *Blood, 90*(12), 5002–5012. https://doi.org/10.1182/BLOOD.V90.12.5002